Characterization and Enhancement of Mechanical Properties in Thermoplastic FFF Parts using In-Situ Annealing

by

Rhugdhrivya Rane

DISSERTATION

Submitted in partial fulfillment of the requirements

for the degree of Doctor of Philosophy in Mechanical Engineering at

The University of Texas at Arlington

August, 2021

Committee Chairman: Dr. Robert Taylor

Supervising Committee:

Dr. Ankur Jain

Dr. Ashfaq Adnan

Dr. Victoria Chen

Dr. Amir Ameri

1

ACKNOWLEDGEMENT

I would like to thank my supervising professor, Dr. Robert Taylor for his continuous support and guidance throughout my PhD journey. I would also like to thank my supervising committee for all their inputs and help. Finally, I would like to thank my lab mate, Manjarik Mrinal for his help in fabricating and testing the parts.

DEDICATION

I would like to dedicate this dissertation to my parents, without their unwavering support and hard

work none of this would have been possible. I also dedicate my dissertation to my brother Flash,

who continuous love has inspired me throughout my journey to become the best version of me.

ABSTRACT

Characterization and Enhancement of Mechanical Properties in Thermoplastic FFF Parts using
In-Situ Annealing

Rhugdhrivya Rane, Ph.D.

The University of Texas at Arlington, 2021

Fused filament fabrication is one of the most common and widely used additive manufacturing
techniques. Owing to its ease of use, availability and cheap feedstock it provides a significant
advantage over other AM techniques. But these advantages are overshadowed by the fact that FFF
parts show high anisotropy and reduced mechanical properties as compared to conventional
manufacturing techniques. Literature review of previous research works show multiple approaches
to enhance the mechanical properties of FFF parts but each of these techniques have limitations to
either the geometries that can be printed or involve complex expensive setups. In one such
technique a metal block is used to apply a thermal field to the part as it is being printed thus
improving the interlaminar bonds and eventually the mechanical properties of the parts. Though
cost effective and simple a major limitation on this technique is that the exposure of the parts to
the thermal field cannot be controlled and has not been optimized. Also, tall and slender parts
cannot be printed due to the lack of a cooling mechanism for the upper sections of the filament.
Another limitation is that of polymer melt leakage around the nozzle which further makes it
difficult to change the nozzle assembly once the block has cooled down. In this project an
optimized print head assembly has been developed to improve the mechanical properties of FFF
parts which addresses the limitations of the previous works while optimizing the mass of the block
and other process parameters to provide maximum enhancement of mechanical properties while
reducing geometric distortions. A design of experiments approach has been used to identify the

main effects and interaction effects between the two factors (Plate thickness and nozzle height) with three levels each for three response variables (increase in UTS, increase in toughness, increase in fracture toughness). The DOE shows that the nozzle height and plate thickness main effects are present for all three response variables. The factor effects on the mechanical properties have further been explained with the help of a finite volume simulation model for the different levels of testing. A cooling mechanism has been provided to the upper sections of the print head to prevent premature filament softening, also a steady state simulation has been conducted along with relevant experiments to check the efficacy of the cooling mechanism. Parts printed with the optimized print head show good correlation with the DOE analysis with major improvements in ultimate tensile strength, toughness, fracture toughness and stiffness of the FFF parts. A study of the mesostructure of these parts show a change in the void shape from a diamond to circular indicating that these voids now behave more as stress concentration zones rather than failure initiation points.

TABLE OF CONTENTS

Chapter 1 Introduction

Manufacturing techniques have been continuously evolving to accommodate fabrication of complex and accurate geometries. Additive Manufacturing (AM) is one such layer-by-layer manufacturing technique which offers the capabilities to produce non-conventional geometries such as topologically optimized, generative designs and functional parts with minimum material wastage [1,2]. AM has shown great promise due to its capability to provide customized and sustainable solutions. [3,4]. The ASTM F42 committee has divided the AM processes into 7 broad categories to obtain standardized terminology. The different AM techniques can be classified as: Material Extrusion (ME), Powder Bed Fusion (PBF), Binder Jetting (BJ), Sheet Lamination (SL), Material Jetting (MJ), Vat photopolymerization (VP) and Direct Energy Deposition (DED) [4]. Each of these techniques have their own special features like material option, speed, resolution and cost, thus offering a wide range of possibilities [5]. Amongst all the AM techniques, the most popular and commonly used technique is Fused Filament Fabrication (FFF) [6]. FFF's popularity can be attributed to its ease of accessibility due to low-cost machines and the availability of a variety of materials commercially [7]. Polymers like polylactic acid (PLA), acrylonitrile butadiene styrene (ABS) [8], polycarbonate (PC) [9], polyether ether ketone (PEEK) [10,11], ULTEM 9085 [12] are the primary feedstock materials used in FFF, also some metal alloys with low melting temperatures can be used [13]. In FFF, a CAD model is used to fabricate parts in a layer wise fashion as seen in Figure 1. Other AM techniques have an energy source that rasters over either a powder bed or photopolymer causing selective fusion to form the final shape [14-18], whereas in FFF a thermoplastic filament is fed into a heated extruder which deposits the polymer melt through

a nozzle at a temperature beyond the glass transition temperature onto a heated build platform [19]. The print nozzle is moved in the x-y plane by a gantry whereas for the out of plane movement the nozzle or bed is moved in the z-direction.
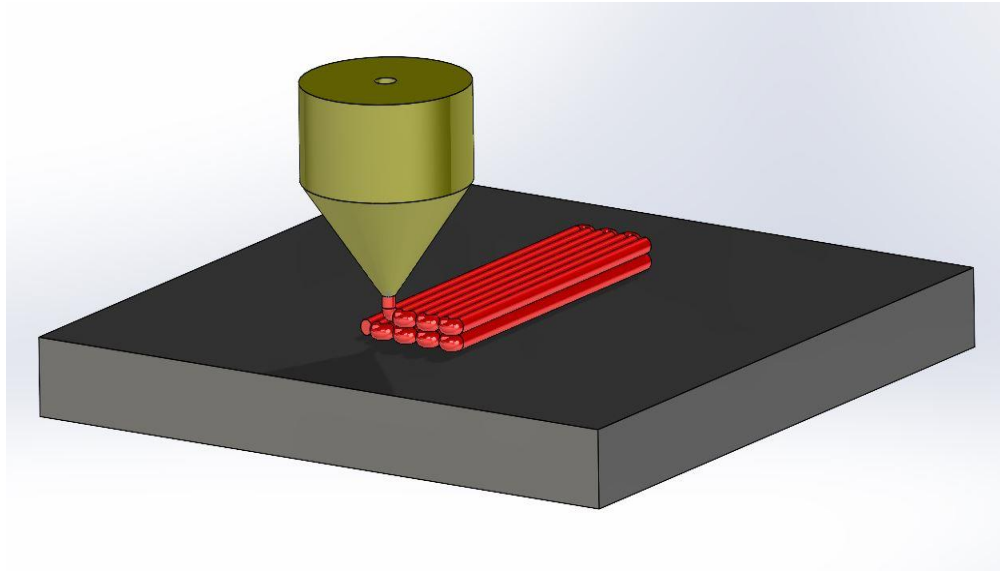

Figure 1. Schematic of the FFF process

In current times FFF has found a wide range of applications like Unmanned Aerial Vehicles (UAV) [20,21], dentistry [22], electrochemical batteries [23], lattice and cellular materials [24–25], sandwich structures [26], tissue engineering scaffolds [27-28], and even printing parts for 3D printers itself [29]. With such a plethora of applications for FFF parts, the characterization of its mechanical properties, has become critical. It is seen that parts fabricated using FFF suffer from a major drawback of reduced mechanical properties [30-32] and are highly anisotropic as compared to their injection molding counterparts and thus cannot be directly used in engineering applications. These reduced mechanical properties and anisotropy of FFF parts limit their use majorly for prototyping and not for the fabrication of end use parts. Thus, to tap into the advantages provided by FFF it is of vital importance to study the parameters that affect the mechanical properties and methods employed to improve these properties.

Studies have shown that the interlaminar bond between the polymer layers dictates the mechanical properties of FFF parts. The interlaminar bond formation in FFF parts has been modeled and described in multiple ways based on polymer interface healing, with the main stages being [33-36]: (1) Heating of the Filament-Filament interface above the glass transition temperature, Tg enabling polymer flow and mobility; (2) Intimate physical contact between the adjacent polymer interfaces (adjacent layers in FFF parts); (3) Thermal polymer healing or diffusion at the interface (4) Cooling of the interface below Tg. Thus, in the FFF process a polymer melt is extruded onto a previously deposited comparatively cooler layer causing the interface to rise initially and then fall rapidly below Tg. The interlaminar regions (weld region) between adjacent filaments are the weakest sections in FFF parts due to this complex thermal history thus leading to premature failures [36]. It is also seen that due to the rounded nature of the deposited polymer melt the presence of voids is an inherent defect of FFF parts thus further degrading their mechanical properties [37-40]. FFF parts have been studied under multiple test conditions like tension [41-45], compression [46-50], fracture [51-55], torsion [38,56] and dynamic loading [57-60] reinforcing the dominant effect of the weak interlaminar bonds on the overall mechanical properties of FFF parts.

Thus, an improvement in the interlaminar bond strength is warranted if FFF parts are to be used for end use applications. In the current work, a print head has been designed such that there is an overall improvement in the mechanical properties. A nozzle with an integrated plate is used which applies a passive thermal load onto the previously printed layers, thus keeping the deposited layers above the glass transition temperature leading to improved bond formation. The print head geometry (plate thickness and nozzle height) are optimized by analyzing the factor effects using a

design of experiments approach. Further a study of the changes in the void structure is done to better understand the improvement in mechanical properties.

Chapter 2 Background

Physics Governing the Interlaminar bond

Previous studies make it clear that improving the interlaminar bonding causes the FFF parts to exhibit enhanced mechanical properties. Multiple models have been developed to explain the factors that influence the interlaminar bonding with most models based on the Reptation theory of polymers [35-36,61]. An ideal condition of bonding between two polymeric interfaces is when both interfaces are heated beyond Tg, while maintaining intimate contact between the surfaces. Now interfacial bond strength is dictated by the number of polymer chains and their distance of diffusion across the polymer interfaces. This interpenetration distance (χ) and length of polymer chain (l) can be predicted using the De Gennes Reptation theory. This diffusion of polymer chains continues till the interface is indistinguishable and the interpenetration distance (χ_∞) becomes equivalent to that of the bulk material at a reptation time tr. Figure 2 shows the schematic of the healing process.

It has also been analyzed that the molecular weight (M) of the polymer chains play a vital role in the interdiffusion process. For very long polymer chains where $M \gg Mc$, which is the critical molecular weight of entanglement the maximum bond strength, σ_∞ can be achieved at weld time t_w instead of the reptation time t_r. Here the interpenetration distance and length of polymer chain at time t_w have values χ_w and l_w respectively. From the work done by Prager et al the healing process is described using a ratio of interface bond strength σ and strength of bulk material σ_∞.

This ratio is called the degree of healing (D_h) and characterizes the bond strength developed [62]. Equation 1 shows the relation between degree of healing and the different parameters defined previously.

$$D_h = \frac{\sigma}{\sigma_\infty} = \frac{\chi}{\chi_w} = \left(\frac{l}{l_w}\right)^{\frac{1}{2}} = \left(\frac{t}{t_w}\right)^{\frac{1}{4}} \tag{1}$$

And t_w was found out by Pitchumani et al by empirically fitting an Arrhenius Energy relation [63] given by:

$$t_w = A \, exp\left[\frac{E}{R}\left(\frac{1}{T} - \frac{1}{T_{ref}}\right)\right] \tag{2}$$

Where A is a constant for fitting, E is the Activation energy, R is the Universal Gas constant and T_{ref} is the reference temperature. These studies provide us with parameters that affect the interfacial bonds between polymers during the healing and diffusion process. Studies by Tirrell et al and Lee et al show that the self- diffusion of the polymer chains during the healing process is dependent on the molecular weight (M) given by [64-65]:

$$D = M^{-2} \tag{3}$$

Where D is the coefficient of self-diffusion of the polymer chains. Further studies regarding the coefficient of self-diffusion show that it is inversely proportional to the viscosity of the polymer melt [66-68]. A higher coefficient of self-diffusion signifies better interfacial bonding during the healing process.

11

T >T$_m$ ... Intimate surface
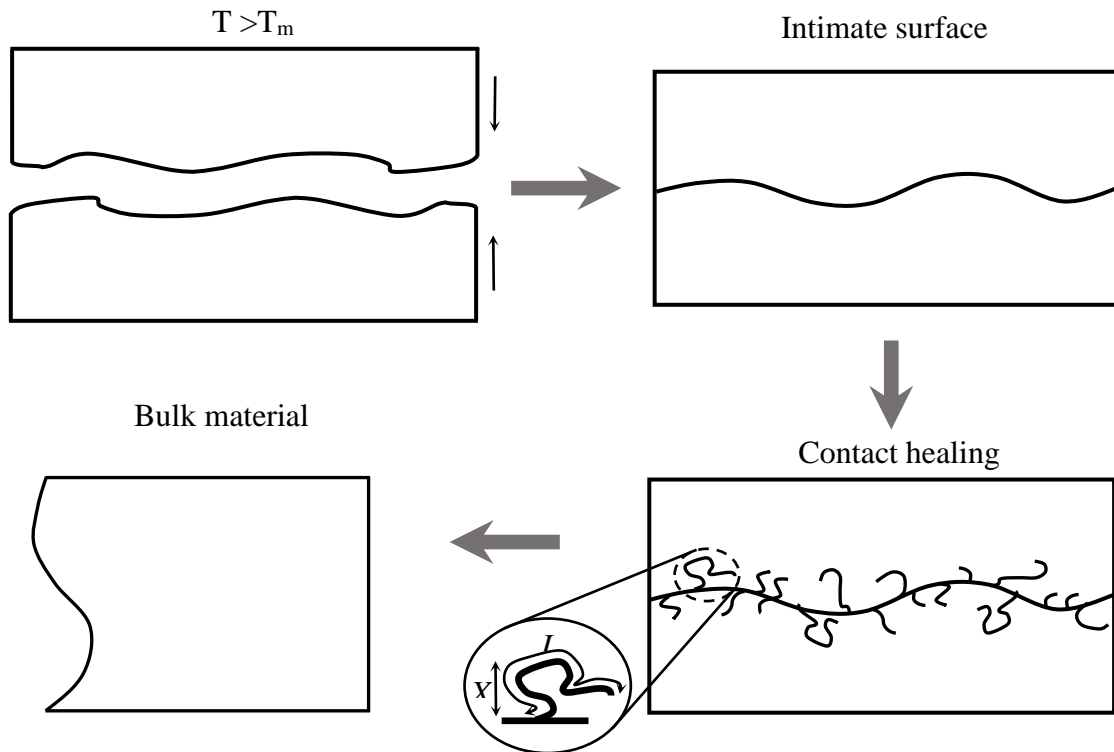
Bulk material ... Contact healing

l

x

Figure 2. Healing process between two polymer surfaces maintained in intimate contact

Thus, it is clear that FFF parts show substantially reduced mechanical properties as compared to conventional manufacturing techniques, and these mechanical properties are dominated by the imperfect weld lines and inter-laminar bonds between adjacent layers. The above mathematical models provide us with parameters that can be optimized to improve these interfacial bonds which are the weakest sections in FFF parts. A variety of techniques have been studied in the past to improve the mechanical properties of FFF part and further sections provide a detailed review of these different methods. The reviewed techniques are categorized as: (1) Pre-processes like optimum print parameter and addition of certain plasticizers to the filaments; (2) In-situ techniques

that are applied as the part is being printed; (3) Post-process techniques like thermal annealing. The systematic review of the different techniques gives insight on the available methods to improve mechanical properties and their shortcomings. Based on the learning from these methods, the proposed project provides a cost effective and optimized solution to improving the mechanical properties while overcoming the shortcomings in the current techniques.

In this review the different techniques used to improve the mechanical properties of FFF parts are divided in 3 broad categories: (1) Pre-Process Techniques; (2) In-Situ Techniques; (3) Post-Process techniques. The pre-process techniques have further been divided into two parts: 1) Print Parameters Effects and 2) Filament Additives and Modifications thus allowing us to cover a wider array of techniques that influence the mechanical properties.

Literature review of Different Techniques to Improve Mechanical properties of FFF parts

Pre-Process Techniques: Print Parameters Effects and optimization

It has been observed that different print parameters like, raster angle, print orientation, filament separation etc. affect the structure of the FFF parts thus influencing the mechanical properties of the parts. In this section the effect of modifying different print parameter on the mechanical properties has been studied. The different parameters which can be modified have been shown in Figure 3. In the figure 3 the print orientation with the have been defined as Upright (U), On Edge (OE) or Flat (F). The FFF parts fabricated have been characterized using tensile, compression and fracture tests with tensile tests being most frequently used. Different filament materials have been studied with the most common being (PLA) and ABS.

Ahn et al and Rodriguez did some of the earliest works under tensile and compressive loading conditions by varying the print parameters [31,38]. Ahn et al, printed dogbone samples based on the ASTM D638 standard with three different raster angles, $\theta=0°$, $45°/-45°$, $90°$ and airgaps varying from a= 0.0 mm to -0.002 mm. It was seen that due to the quasi-solid nature of the samples there was almost no penalty in stiffness on varying the print parameters. This has also been reported by Durgan et al with the underlying reason being that 100% density FFF parts tend to be free from voids due to reduction in porosity [76]. Durgan et also suggested that the effect of build orientation was more significant than the raster orientation of the parts. Rodriguez et al fabricated parts with negative as well as positive air gaps with skewed layer stacking. In skewed layer stacking the adjacent layer rasters are staggered to be placed in the midpoint of the rasters of previous layer. It was seen that for positive air gaps a fall in stiffness of 11-37% is observed. The maximum difference is seen for parts printed with positive air gaps. Durgan et al observed that the

14

tensile strength of the parts was much more affected by the defects in the sample and the build orientation with maximum tensile strength found for parts with raster orientation along the loading direction. It is seen that parts printed with 100% density have significantly less voids as compared to parts with positive air gaps. Parts with positive air gaps print much faster and are lighter than the completely dense parts but the mechanical properties of these parts are penalized.

Montero et al [77] studied 5 different process parameters: air gap, extrusion temperature, filament color, raster orientation and raster width. The samples were printed with an ABS filament and the results showed that air gap and raster orientation played a major role in the tensile strength of the parts, and for maximum tensile strength a negative air gap and raster orientation of 0° should be maintained. Es-Said et al modified the raster orientation to show that a 0° raster orientation allows best results for tensile strength [78]. Studies by Zaldivar et al [79] and Wang et al [80] reported that the build orientation in the z-direction was the dominant factor in improving tensile strength of the parts. Panda et al [81] studied the effect of 5 parameters namely, layer thickness, raster width, build orientation, raster orientation and build orientation and concluded that all the parameters influence the tensile strength of the parts except for the raster width. Gorski et al studied the effect of build orientation on ABs parts and concluded that the build orientation of 0° was optimum for tensile strength [82]. Gorski also noted that for build orientations exceeding 20° and 25° in the X and Y axis respectively the parts exhibited brittle failure. A study by Wittbrodt et al analyzed the effect of PLA filament color and printing temperature on the tensile strength of FFF parts. 4 colored filaments were used (white, grey, blue, black) and were printed at two different temperatures (190° C and 200°C) and 100% density. No statistical effect of color was found on

the tensile strength of the parts, but it was seen that the PLA color affects the part crystallinity [83].
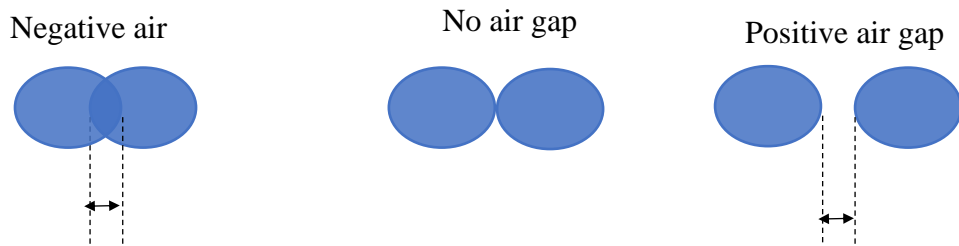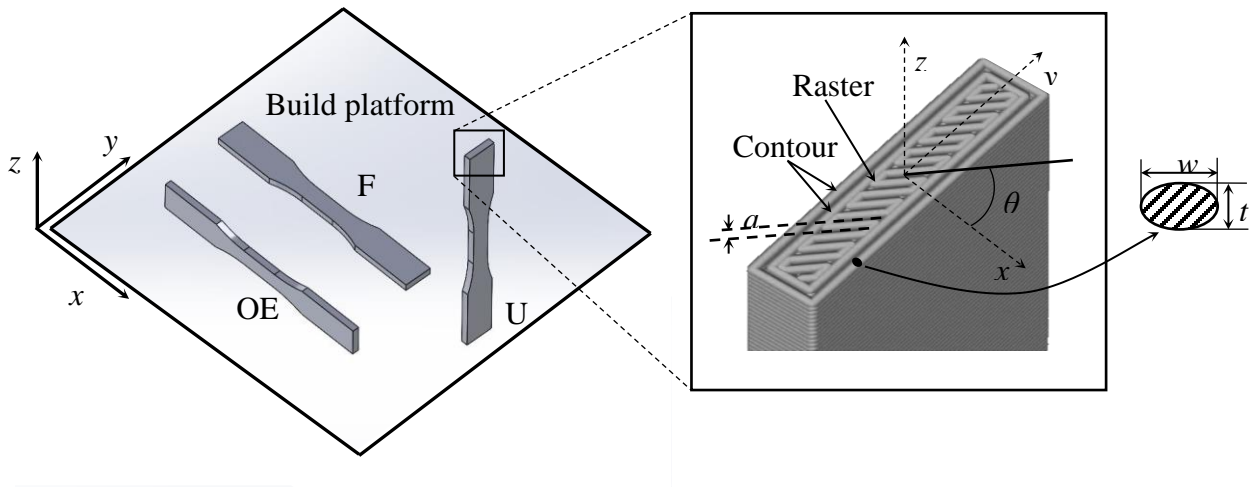

Figure 3. Different print parameters that can be varied during FFF

Deng et al used a design of experiments (DOE) approach to study the effect of print speed, infill density, layer thickness and print temperature on PEEK samples and found that best results for tensile strength were found for a print speed of 60 mm/s, layer height 0.2mm, infill density of 40% and print temperature 370°C [84]. Uddin et al studied the effect of three values of layer thickness on stiffness and strength of 100% dense ABS parts [85]. He observed that the samples with thinnest layer thickness showed maximum values of stiffness and strength. Sood et al used a DOE approach to study the effects of five print parameters (layer thickness, raster orientation,

build orientation, raster orientation and raster width) [86]. Using ANOVA, it was seen that all parameters except raster width had significant main effects on the tensile strength with the presence of some interactions. Another study by Sood et al [47] studied the effect of layer thickness, print orientation, raster width, air gap and raster angle on the compressive strength of FFF parts. It was observed that a reduction in layer thickness, raster width and air gap lead to an increase in strength.

It is seen that most characterization methods include tensile testing of the FFF parts, but most end use parts are under a combined loading condition. Thus, it is also important to understand the fracture behavior of FFF parts and the parameters that affect it. Aliheidari et al studied the mode-I fracture in fully dense double cantilever beam (DCB) ABS specimens [55]. The raster orientation was aligned to the longitudinal axis of the cantilever beams. The specimens were printed at three different print temperatures (210°C, 230°C, and 240 °C). The energy release rate for mode-I fracture was calculated using the J-integral method. An increase in print temperature showed increased fracture resistance due to enhanced bonding between layers. This enhanced bonding can be explained by the dependance of degree of healing on the temperature as seen from the models explained previously. Hart et al studied the influence of raster angle and orientation on the fracture properties of ABS specimen [87]. The specimens were printed Upright (U) and Flat (F) to study the effect of fracture between two layers and across layers. It is seen that to energy required propagate the crack across layers was an order of magnitude higher than that needed to propagate the crack between layers. It was seen that across layers there was ductile behavior during fracture whereas between layers the specimen exhibited brittle behavior.

Table 1 summarizes the effect of print parameters on the mechanical properties. Thus, from the literature review of the effect of print parameters on FFF parts it was seen that for tensile

strength the build orientation played the most prominent role. The maximum tensile strength was found to be when the rasters were aligned with the loading direction, thus a raster angle of 0° in the Flat or On-edge orientations. On the contrary the build orientation has little effect on the compressive strength of FFF parts. It is seen that layer thickness has an interaction with other parameters like part orientation, but it is suggested to have small layer height for better surface finish and tensile strength. Another important parameter is the print temperature of the FFF parts. Research shows that higher print temperatures lead to reduced viscosity and increased fluidity of polymer melt, thus increasing the interlaminar bonding. Thus, for better tensile or fracture strength a high print temperature is preferred. However, for improved compressive strength a higher value of layer height is preferred. Infill density is another important print parameter that has a positive correlation with the tensile strength of the parts. A high infill percentage increases the bonding area and leads to stronger interfacial bonds.

Table 1: Summary of pre-process approaches to improve mechanical properties

Authors	Mech. Properties	Raster Angle	Part Orientation	Filament Material	Layer height (mm)	Air Gap	Raster width	Print Speed (mm/s)	Print Temperature (°C)	Infill Percentage	Test	Conclusions
Ahn et al. [31]	Strength	0, 45/−45, 90, 0/90	U, F	ABS	-	0 mm, -0.002mm	-	-	260,280	100	Tension, Compression	Air gap and raster orientation affect tensile strength
Durgan et al. [76]	Stiffness, Tensile strength	0, 30, 45, 60 and 90	U, F, OE	ABS	0.254	-	-	-	-	100	Tension, Flexural	Part orientation has greater influence on mechanical properties as compared to raster angle. Small raster angle (0°) gives higher strength
Montero et al. [77]	Tensile Strength	0/ 90, 45/-45	F	Blue and White ABS		0 in, -0.002 in	0.02 in, 0.0396 in		270, 280	100	Tension	Air gap and raster orientation have dominant effect on tensile strength. Negative air gap increases tensile strength
Zaldivar et al. [79]	Tensile Strength	-	U, F 0°, F 90°, OE, OE 45°, F 45°	ULTEM 9085	0.254	-	-	-	-	100	Tension	Build orientation with higher fraction of raster aligned in the loading direction show enhanced strength
Wittbrodt et al. [83]	Tensile Strength	0/90	U	white, grey, blue and black PLA	-	-	-	-	190	100	Tension	Color affects crystallinity of the parts but little effect on strength
Deng et al. [84]	Tensile Strength	-	-	PEEK	0.2, 0.25, 0.3	-	-	20, 40, 60	350, 360, 370	20, 40, 60	Tensile, Flexural	A print speed of 60 mm/s, layer height 0.2mm, infill density of 40% and print temperature 370°C gives maximum tensile strength
Uddin et al. [85]	Tensile/ Compressive Strength, Stiffness	-	U, F, OE	ABS	0.09, 0.19, 0.39	-	-	-	245	100	Tension, Compression	Smaller layer height shows higher strength and stiffness
Sood et al. [47]	Compressive Strength	0, 30, 60	U	ABS	0.127, 0.178, 0.254	0.4064	-	-	-	-	Compression	Maximum compressive stress of 17.4751 MPa obtained at the optimum value of layer thickness 0.254, orientation 0.036°, raster angle 59.44°, raster width 0.422 and air gap 0.00026 mm
Aliheideri et al. [55]	Fracture toughness	0	U	ABS	0.2	-	0.35	-	210, 230, 240	100	Mode I Fracture	Higher print temperatures increase fracture resistance of parts
Hart et al. [87]	Fracture toughness	0/90	U, F, Obliquely		0.22			50	240	100	Mode I Fracture	Brittle interlaminar failure and Ductile cross laminar failure was observed

It is seen that with pre-process techniques a stagnation point is reached with respect to the improvement in the mechanical properties. In-Situ techniques are treatments that influence the part while part fabrication is in progress to improve the interlaminar bonds thus improving mechanical properties. The in-situ techniques have been divided into two broad categories: a) Use of an energy source to improve bonding; b) Filament material modifications. Filament material modifications is a quasi in-situ technique because most changes to the filament are part of the pre-process stage in FFF, but multiple techniques also employ methods to add fillers or fibers while the part is being fabricated thus making it a quasi in-situ process.

Use of an Energy Source to Improve Bonding

Past research has shown the importance of temperature in the quality of bond formation; thus, most in-situ techniques aim at applying a thermal load to improve bond quality. Initial stages of in-situ techniques using energy sources involved the use of a heated chamber where the entire build is in an envelope of hot air. Yang et al studied the effect of ambient temperature on the tensile strength of the parts by maintaining the ambient air at five different temperatures (25°C, 50°C, 100°C, 150°C and 200°C) [88]. The increase in ambient temperature led to increased crystallinity from 17% to 31% and an increase in the elastic modulus and tensile strength of the parts. In a study done by Kuo et al. an elevated chamber temperature to 43°C showed a reduction in the warpage of the parts [89]. But it has also been seen that a very high chamber temperature could have negative effects on the geometric accuracy of the parts.

Ravi et al. introduced a novel technique which applied a local pre-deposition heating using a near-IR laser [90]. The near-IR laser applies a focused thermal load on the previously existing

ABS layer thus accentuating the wetting and diffusion process resulting in better bond quality and improved mechanical properties. In this study a 50% increase in interlayer bond strength and increased ductility was observed, also as the laser-based pre-heating is localized the dimensional accuracy of the parts is not compromised. Kishore et al used infrared (IR) radiation on the Big Area Additive Manufacturing (BAAM) system to preheat the previously deposited surfaces before depositing a new layer on it [91]. IR lamps were used to preheat the layers of large hexagonal components at 3 different print speeds and heating settings. DCB specimen harvested from these large hexagons more than double average fracture energy in some cases. In the work done by Sweeney et al. the filament is initially coated with multi-walled carbon nanotubes rich polymer (MWCNT), printing these filaments leads to a macroscopic structure with MWCNT on the interfaces [92]. When these parts are exposed to microwave irradiation the interfaces loaded with MWCNT selectively heat up leading to enhanced diffusion at polymer interfaces. In the study the fracture strength increased by 275% and the parts exhibited ductile behavior. Ravoori et al. subjected FFF parts to in-situ annealing by attaching a heated metal block to the extruder setup [93]. This metal block heats up the previous layers via conduction and convection above the T_g thus accentuating wetting of the previous layers and resulting in enhanced diffusion of polymer chains across the interface. The toughness of the parts increases by 165% and the tensile strength by 60%. Another study by Shih et al. utilized cold plasma treatment (CPT) to enhance the interlaminar bonding [94]. The CPT triggers oxidation on polymer surfaces, forming high surface energy carbonyl groups on the surface, leading to an improvement in the wettability. CPT breaks the polymer chains on the surface proving loose ends for better quality bonds. This technique led to the increase in bond strength by 100%. Figure 4 shows the setups for the different energy sources used in in-situ processes.

Table 2 summarizes the different in-situ techniques used to improve mechanical properties. It is seen that in most in-situ techniques different energy sources are used to apply a thermal load on the previously deposited layers to improve interface bond quality. Though the results of in-situ techniques are promising they require the use of complex and expensive setups thus inhibiting their use. The literature review also shows that the reference specimen in most in-situ techniques do not use optimized print parameters to fabricate the parts thus showing to inflated values of increase in mechanical properties after the use of in-situ techniques. Also, a detailed study of their effect on geometric accuracy needs to be done to better understand their scope of use in actual end use parts.

Table 2: Summary of In-situ approaches to improve mechanical properties

| Authors	Energy source	Conclusions	Limitations
Yang et al. [88]	Heated Chamber	Results in increased crystallinity from 17% to 31%. Increase in stiffness and tensile strength	Dimensional accuracy is difficult to maintain.
Ravi et al. [90]	Near-IR laser	50% increase in interlayer bond. Reduced geometric distortion.	Complex and expensive setup involving moving mirrors.
Kishore et al. [91]	IR radiation lamps	Almost doubles the fracture energy in some cases. Can be used with BAAM components to print end use parts.	Complex and expensive setup.
Sweeney et al. [92]	Microwave radiation	Increases fracture strength by 275% and increase in ductility of parts.	Additional setup required for coating the filament with MWCNT.
Ravoori et al [93]	Heated block	Increased tensile strength by 60% and toughness by 165%	Dimensional accuracy is penalized. Inability to print tall and slender parts
Shih et al. [94]	Cold Plasma	Bond strength improved by 100%	Surface treatment of specimen needed before CPT can be applied. Complex and expensive setup.
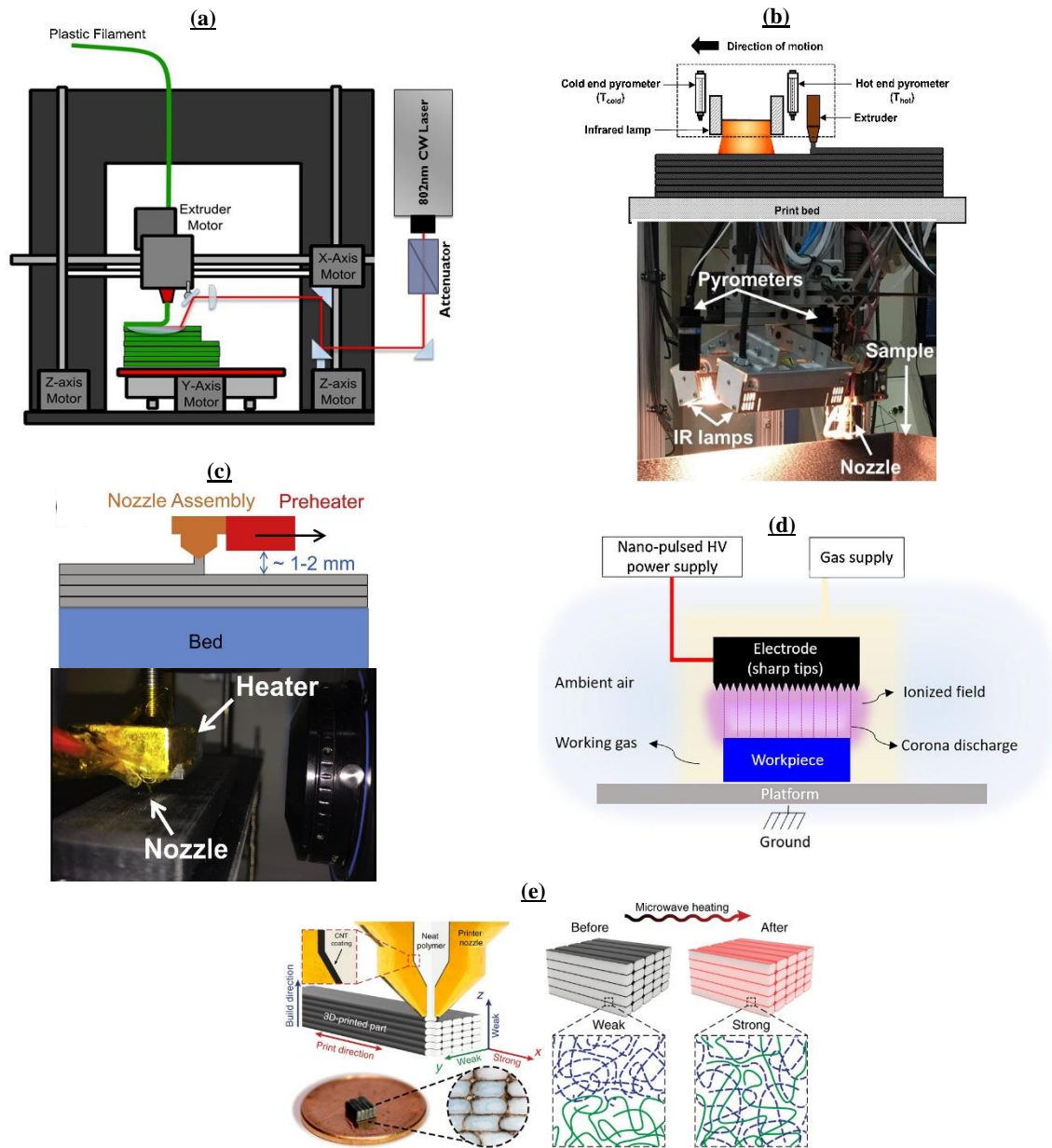
Figure 4. Setups for In-situ techniques using (a) Laser heating [90] (b) IR radiation [91] (c) Metallic block heater [93] (d) Cold Plasma [94] and (e) Microwave irradiation [92].

Filament Material Modifications

Various filament materials have been studied to characterize their effect on the mechanical properties of FFF parts. FFF materials can be divided into single materials, reinforced composites and polymer blends. The most researched materials of these are the single materials which include the most common commercially available filaments like PLA and ABS. Studies have shown that some single materials show enhanced mechanical properties as compared to their counterparts. Polyetherether ketone (PEEK) is one such material that has been researched extensively. A comparative study between PEEK and ABS by Wu et al, showed that the tensile strength and elastic modulus of PEEK was 122% and 108% higher than that of ABS [95]. Another study by Boschetto et al uses Polycarbonate (PC) filament in FFF to obtain a tensile strength up to 68 MPa [96]. Cantrell et al did a characterization study for PC and ABS parts which showed that for similar build orientation PC exhibits almost double the strength of ABS parts [97]. ULTEM 9085 is another high-performance polymer that has been widely researched due to its high strength to weight ratio facilitating its use in aerospace industries [98].

It should be noted by the reader that while studying the data reported in this section, apart from the materials and setup used the processing conditions and printing parameters play an important role in defining the mechanical properties of the FFF parts. The objective of this section is to only provide a general overview of the effect of composite filament materials on the mechanical properties of FFF parts. Reinforced composite materials have been studied extensively due to their ability to print functional FFF parts. Different forms of fiber reinforcement, namely continuous and discontinuous are used in the filament material of FFF parts to improve their mechanical strength. In continuous fiber reinforced polymers, the material is directly fed into the

FFF setup to achieve impregnation of the fibers into the polymer matrix. Two kinds of FFF setups are used to print continuous fiber reinforced FFF parts. The first where the fiber is merged with the polymer melt pool in the extrusion chamber and then the polymer coated fiber is extruded via a single nozzle [99,100]. The fiber could be chemically treated before impregnating it into the polymer matrix [101]. The second setup is where the polymer is deposited with one nozzle and the second nozzle extrudes the fiber impregnating it into the polymer matrix. Literature review of these approaches show that different setups along with different combinations of fibers and polymer matrix provide improvements in various mechanical properties of FFF parts. In the work done by Hao et al carbon fibers were impregnated in an epoxy melt to achieve a tensile strength of 792.8 MPa which is significantly higher than the strength seen for single material FFF parts [99]. Another study by Akhoundi et al uses glass fibers in a PLA melt to achieve a tensile strength of 479 MPa [100]. Oztan et al studied the effect of Carbon fiber and Kevlar fiber in a Nylon matrix to achieve a tensile strength of 250.8 MPa and 150.2 MPa respectively [102]. Matsuzaki et al showed that the use of heated synthetic carbon fibers leads to higher diffusion of the fibers in the PLA matrix resulting in a tensile strength greater than 220 MPa [103]. The study also showed that even though the tensile strength of the parts increased the parts showed brittle behavior. It is also seen that the tensile properties depend on the quality of fiber wetting and the fiber volume fraction achieved during the printing process. Most studies show that high tensile strength can be achieved using carbon fibers, but a study by Li et al shows that a high carbon fiber content of 34% by volume in a PLA matrix yields a strength of only 91 MPa due to poor wetting of the fibers [104]. Figure 5 shows different setups used in the fabrication of FFF parts using continuous fiber composites. A limitation of continuous fiber reinforced printing is that only a limited amount of continuous fibers

26

can be impregnated into the matrix, also the wetting of the fibers poses another problem and may lead to fiber pullout [105].

In addition to continuous fiber reinforced composite materials, discontinuous fiber reinforced materials have also been widely studied. In discontinuous fiber reinforced materials, most of the fibers align in the direction of the polymer road deposited, thus yielding the highest mechanical properties in these directions. Gardner et al reinforced polyertherimide (PEI material) with 4.7% by weight carbon nanotubes (CNT) to achieve a strength of 123.5 MPa [106]. Multiple studies have been done with ABS as the base with carbon fiber reinforcements to achieve tensile strengths in the range of 30 to 70 MPa and tensile modulus between 2 to 15 GPa [107]. Studies have also shown that for discontinuous fiber thermoplastic materials the strength is much lower (5 to 10 MPa) as compared to epoxy systems (45 MPa). This can be

justified because of the lower viscosity of epoxy systems the laid down beads are wetted more easily leading to better bonds. In a study done by Hassen et al, polypropylene sulphone (PPS) is reinforced with carbon fibers for BAAM resulting in high mechanical strengths. Even though both continuous and discontinuous fiber reinforced materials have shown enhanced strength when the loading direction is aligned with the fiber orientation, an application of a transverse load shows almost no improvement due to the impregnated fibers but rather the strength is dominated by the interfacial bond quality.
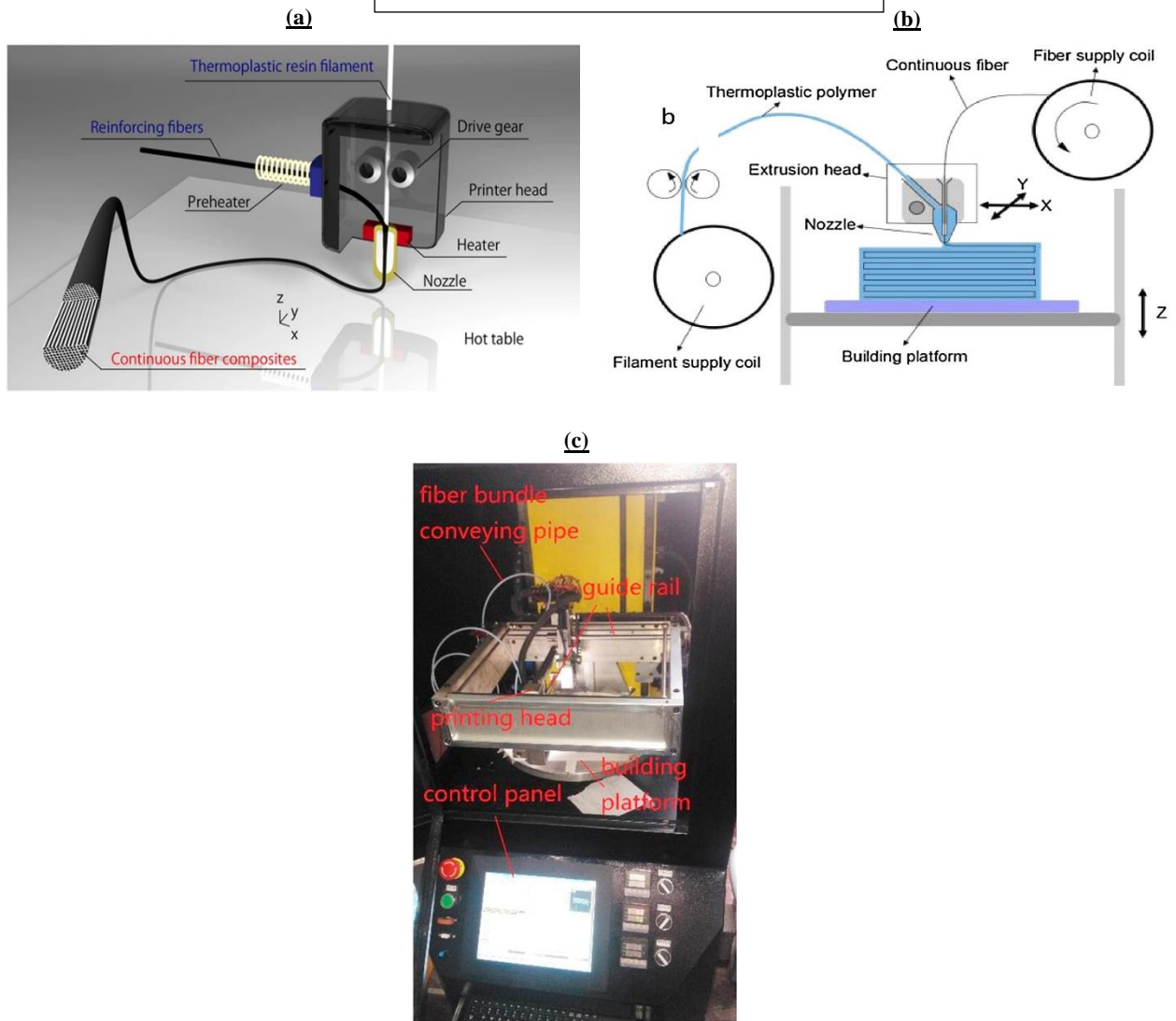
Continuous Fiber Composites

Figure 5. Continuous fiber composites setups created using (a) heated fiber [103] (b)untreated [88] and (c) carbon fiber impregnated in polymer melt [99].

An innovative approach in the filament modification approach has been the blending of different polymers. Most polymer blends for FFF are made by melting the blends together or reactive extrusion of the polymers in the presence of plasticizers [108], compatibilizers [109,110] and molecular chain extenders [111]. ABS and styrene ethylene butylene styrene (SEBS) blends

28

have shown improvement in mechanical strength and ductility as compared to pure ABS. Models explaining the bond formation in FFF parts have shown molecular to be a significant factor affecting the interfacial bond. In works done by Levenhagen et al, low molecular weight segregation additives (LMW-SuSAs) were added to the ABS and SEBS blend leading to an improvement in the interfacial bonds of the blend [112-114]. Another study by Levenhagen et al showed that a blend of ABS and styrene acrylonitrile resulted in improved tensile strength as compared to pure ABS [114].

The literature review shows that modifications to the filament materials can lead to significant improvements in mechanical properties. But a major limitation of modifications to the filament material is the difficulty in printing parts. For example, PEEK and Nylon provide improved strength but they are difficult to print due to shrinkage issues and their inability to stick to the bed easily. Polymer composites show improvement in mechanical properties only in the direction of alignment of the fibers thus limiting their use. Thus, further research needs to be undertaken to address these issues and develop filament materials that are not only superior in mechanical properties but are also easy to print.

\

Post-Process Techniques

Post-process approaches involve applying treatments to FFF parts once they have been fabricated. Most post process techniques involve either chemical treatments of the parts or exposing them to an energy source to influence bond quality. Initial studies in post- process methods by Galantucci et al, involved the treatment of FFF parts with a mixture of 90% acetone and 10% water [115]. This improved the surface finish of the parts but lead to a slight fall in tensile and flexural strength. A study by Li et al treated short carbon fiber with nitric acid to improve the bond strength with ABS [116]. Literature review shows that most chemical treatment of ABS parts leads to improved surface finish but a drastic fall in tensile strength, thus rendering it of little use [117-118].

Apart from chemical treatments multiple innovative post-process techniques have been used to improve the interfacial bond in FFF parts. In a study by Lederle et al, the FFF sample was printed in a nitrogen gas envelope which resulted in a 30% improvement in tensile strength for both PLA and ABS samples [119]. Chen et al applied a laser treatment to a Cu fiber composite in PLA matrix, thus improving the tensile strength and elastic modulus of the parts by 25.6% and 34.1% respectively [120]. This treatment lead to better bonding between the fiber and the matrix while eliminating the voids in the FFF parts due to polymer chain breakdown flow of molten material into the voids. Thus, by using laser treatment under favorable conditions significant improvements in tensile strength can be achieved.

(a)

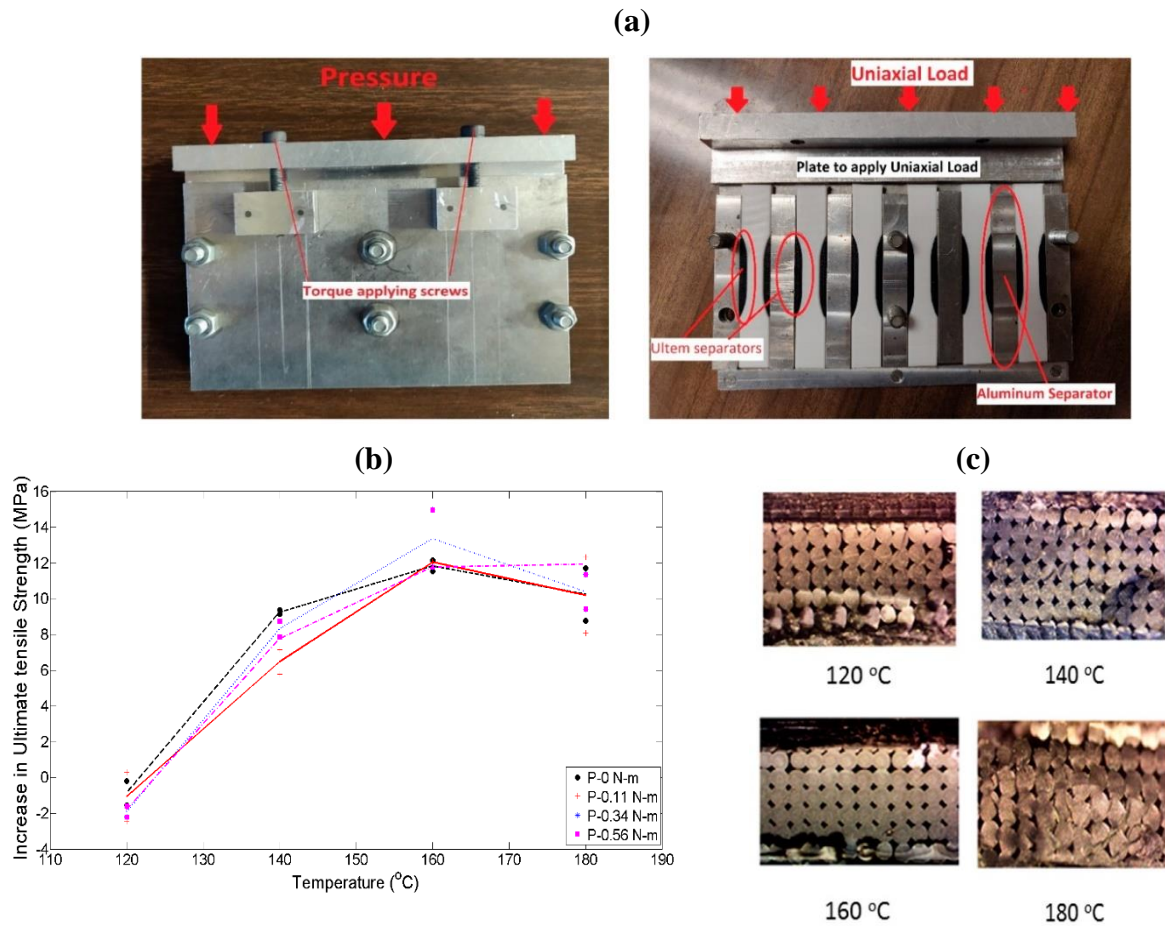**(b)**   **(c)**

Figure 6: Thermal annealing of ABS parts accompanied with a uniaxial load [121,122] . (a)

Setup (b) Plots showing increase in ultimate tensile strength with annealing temperature. (c)

Increase in bond length with annealing

The most common and popular post process technique to improve mechanical properties is thermal

annealing of the parts. Bond formation models show that the quality of the bond depends on the

intimate contact between layers and the diffusion of polymer chains across the interface. Rane et

al studied the effect of annealing temperature and initially applied static load on the tensile strength of the FFF parts for four levels of annealing temperature and uniaxial pressure by using the setup shown in Figure 6. It was seen that the annealing temperature is the dominant factor in influencing bond strength. A tensile strength increase of up to 89% was observed in the ABS samples whereas an increase in ductility of the parts was also seen [121-122]. Figure 6 also shows the change in the bond length and void structure with an increase in annealing temperature. An increase in annealing temperature shows an increase in bond length up to 160°C thus leading to an increase in ultimate tensile strength. Singh et al studied the effect of annealing temperature and time on the mechanical properties of FFF parts. It was seen that an increase in annealing temperature had a major impact on the mechanical properties, whereas the annealing time was found to be less significant [123]. Hong et al showed that thermal annealing increased the flexural and compressive strength of parts [124].

Hart et al studied the effect of thermal annealing on the fracture toughness of amorphous FFF parts [125]. The single edge notched beam (SENB) samples were exposed to different levels of annealing temperatures and times. For 175°C and 18 hours annealing time a n increase in fracture toughness by 2500% was seen. Another study by Hart et al studied the effect of thermal annealing on semi-crystalline thermoplastics [126]. It was observed that on quenching after thermal annealing the PLA adopts an amorphous nature resulting in almost double fracture toughness and increased ductility. But if the parts were slow cooled after annealing the parts were in semi-crystalline state and shower lower fracture toughness and brittle nature. Thus, thermal annealing has shown to improve the inter-laminar bonds significantly making it an important post-process technique. But a major limitation of thermal annealing is that it leads to geometric distortions of

the part thus making it difficult to maintain tolerances. Hart et al addressed this issue by using a dual thermoplastic filament made of ABS with a Polycarbonate core and then exposing them to thermal annealing [127]. The filament is formed by initially printing a preform structure made up of ABS with a PC core as seen in the Figure 7. This preform is preheated and then pulled to form the filament with the desired core geometry. As seen in Figure 7 parts printed with the dual thermoplastic filament did not show any gravitational creep after thermal annealing thus maintaining geometric accuracy. A significant increase in toughness was also seen in the samples that were exposed to thermal annealing.

Hart et al studied the effect of thermal annealing on the fracture toughness of amorphous FFF parts [125]. The single edge notched beam (SENB) samples were exposed to different levels of annealing temperatures and times. For 175°C and 18 hours annealing time a n increase in fracture toughness by 2500% was seen. Another study by Hart et al studied the effect of thermal annealing on semi-crystalline thermoplastics [126]. It was observed that on quenching after thermal annealing the PLA adopts an amorphous nature resulting in almost double fracture toughness and increased ductility. But if the parts were slow cooled after annealing the parts were in semi-crystalline state and shower lower fracture toughness and brittle nature. Thus, thermal annealing has shown to improve the inter-laminar bonds significantly making it an important post-process technique. But a major limitation of thermal annealing is that it leads to geometric distortions of the part thus making it difficult to maintain tolerances. Hart et al addressed this issue by using a dual thermoplastic filament made of ABS with a Polycarbonate core and then exposing them to thermal annealing [127]. The filament is formed by initially printing a preform structure made up of ABS with a PC core as seen in the Figure 7. This preform is preheated and then pulled to form

the filament with the desired core geometry. As seen in Figure 7 parts printed with the dual thermoplastic filament did not show any gravitational creep after thermal annealing thus maintaining geometric accuracy. A significant increase in toughness was also seen in the samples that were exposed to thermal annealing.
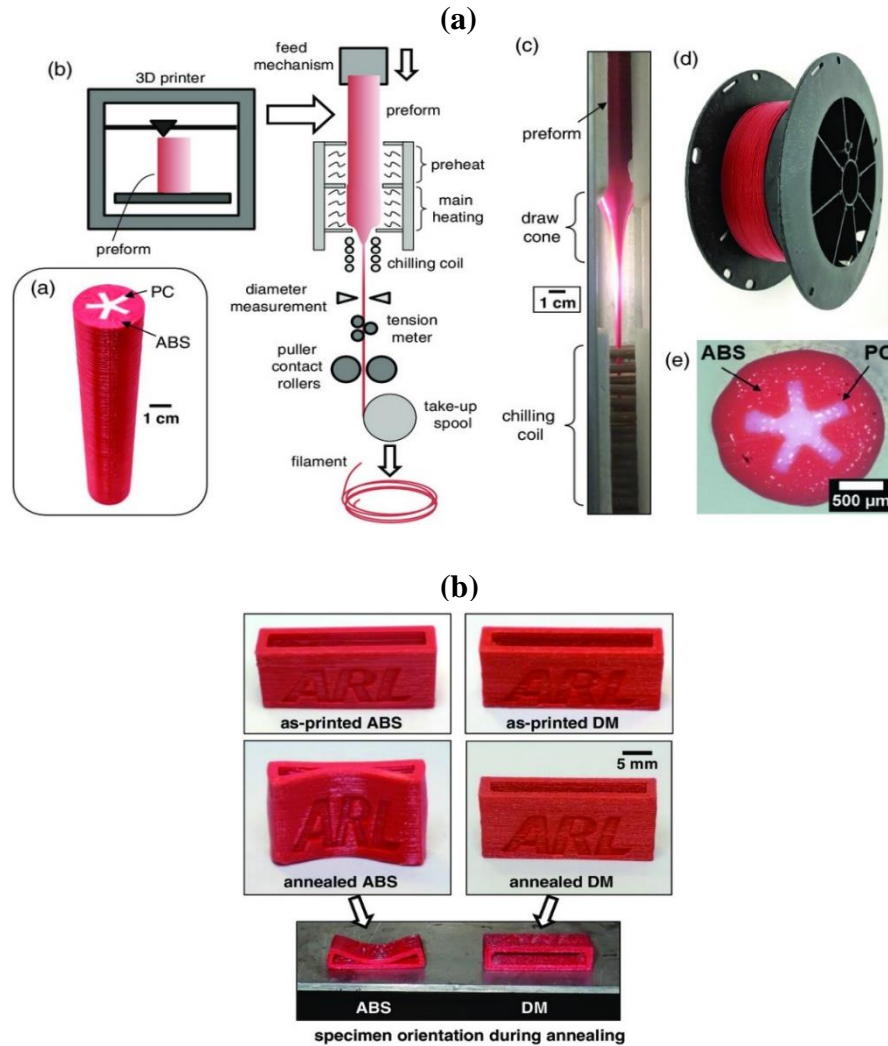

Figure 7. Post process annealing of dual thermoplastic filament [127]. (a) Process to form the dual thermoplastic filament. (b) Lack of gravitational creep after thermal annealing.

Another post-process treatment for FFF parts is the use of ultrasound to improve bond quality. As this is a non- chemical and non-thermal process its adverse effects on geometry are insignificant.

Maidin et al studied the impact of horizontal ultrasonic vibrations on ABS parts while it was printing [128]. A significant increase in tensile strength was observed accompanied by a decrease in layer thickness by 0.02 mm. Another study by Tofganchi et al applied ultrasonic vibrations via a piezoelectric bolt clamped transducer to the heating block of the print head [129]. A 10% increase in layer adhesion was observed in the treated parts. But ultrasound as a post process approach was studied by Wu et al, by applying a pressure using it onto a completed FFF part [130]. It is observed that the modulus and bending strength increased by 12.5% and 10% respectively. The ultrasound vibrations are transformed into friction which result in fusion of the adjacent layers due to the heat generated. Thus, ultrasound is an important post process technique that causes enhanced mechanical properties due to its ability to not cause any chemical changes in the part while maintaining geometric accuracy.

Thus, the literature review suggests that post-process techniques have a major impact on the mechanical properties of FFF parts, but they also suffer from some major limitations. Table 3 summarizes the different post-process techniques Thermal annealing has shown the most promise in post-process techniques, but using this approach defeats the purpose of using FFF parts. Annealing leads to major geometric distortions thus limiting the approach to very simple geometries. Dual thermoplastic filament accompanied by thermal annealing addresses this problem but the inability to produce the filament in large quantities and the extended time required to form the filament hinders the use of this technique. Further research also needs to be done in the application of ultrasound approach to identify the optimum parameters that would provide the best mechanical properties.

Table 3: Summary of post-process approaches to improve mechanical properties

Authors	Post-Process approach	Conclusions	Limitations
Li et al. [116]	Treat short carbon fiber with nitric acid	13.8% and 164% increase in tensile and flexural strength of parts	Require additional setup to extrude continuous fiber filament.
Chen et al. [120]	Laser treatment to a Cu fiber composite in PLA matrix	Tensile strength and elastic modulus of the parts by 25.6% and 34.1%.	-
Rane et al. [122]	Thermal annealing with uniaxial pressure	Up to 89% increase in the tensile strength of the parts.	Major geometric distortions in the treated samples
Hart et al. [125]	Thermal Annealing of amorphous polymers for different annealing temperatures and times	Increases fracture strength by 2500% for 175°C and 18h.	Major geometric distortions in the treated samples.
Hart et al. [126]	Thermal Annealing of semicrystalline polymers for different annealing times	Significant increase in fracture toughness and ductility when parts are quenched due to locking of the polymer in an amorphous state. Reduced fracture toughness when the part is slow cooled, showing brittle behavior.	Major geometric distortions in the treated samples.
Hart et al. [127]	Thermal annealing of dual thermoplastic filament (ABS/PC)	Increased fracture toughness of the parts. No gravitational creep and significantly reduced geometric distortions.	Difficulty in producing large quantities of the dual thermoplastic filament.
Wu et al	Applying a pressure on finished FFF parts using ultrasound	Modulus and bending strength increased by 12.5% and 10% respectively	Relatively complex and expensive setup is required

Summary and Insights

The techniques and methods reviewed above are based on three broad categories, namely pre-process, in-situ and post process techniques. Each of these categories have been studied extensively for their advantages, effects on various mechanical properties and the limitations to the use of these techniques. A summary of the findings of the review are given below:

Pre- Process Methods

•   The literature review shows that most widely researched category is the pre-process techniques which involves studying the effect of print parameters and their optimization.

•   From the review it is seen that the most significant print parameter is the part orientation. The part orientation has a major influence on almost all mechanical properties. Orientation of the part in a way where the rasters are aligned parallel to the loading directions provides the maximum tensile strength to the parts. But it should be noted that orientation of the parts cannot always be controlled to provide maximum strength while fabricating complex parts because real world applications generally require parts that can withstand loads in multiple loading directions. It is also seen that print orientation has little effect on the compressive strength of the parts.

•   The air gap also plays a major role on the strength and it has been studied that a negative air gap value provides enhanced mechanical properties in FFF parts.

•   Studies show that ABS parts printed with infill density of 100% show higher stiffness and strength values. But one of the advantages of FFF parts is optimization for weight, thus always printing completely dense parts defeats this purpose.

•   Print temperature is another parameter that influences the tensile and fracture toughness of the parts, a higher print temperature leads to better bonding and thus better strength. Excessively high print temperatures also lead to material degradation and geometric distortions in the FF parts.

- In most DOE studies reviewed, layer height is seen to have little effect on the mechanical properties but some studies suggest keeping a smaller layer height for higher tensile strength and a larger layer height for enhanced compressive strength.

In-Situ Methods

- The in-situ methods are divided based on either the use of an energy source while printing or filament modifications before or as we print.

- Multiple energy sources like laser, IR radiation and heated metallic block are used while the part is being printed. These sources provide thermal energy to the previously deposited layers thus improving the bond quality and strength. A major disadvantage of using laser and IR radiation is that the setup is expensive and multiple moving parts need to be controlled. For the heated metal block though the setup is cheap to fabricate, the control on the amount of thermal energy the part is exposed to is limited, thus preventing the setup from printing tall geometrically accurate parts.

- Using energy sources like cold plasma and microwave radiation also enhances the mechanical properties of the FFF parts, but the filament needs to be pre-treated or coated with another material to obtain the desired enhancement. Like most in-situ methods the setups here are relatively expensive. As compared to the energy sources that utilize thermal energy, these methods show comparatively lower enhancements in strength.

- Multiple single filament materials have been reviewed, some of which show substantially enhanced strength. ULTEM 9085 is one such material that shows better mechanical properties as compared to other stock filaments accompanied by a greater resistance to thermal distortion. Using PEEK as the filament material has shown to give a 122 % increase in strength of the parts.

• Another in-situ method used in the works reviewed is filament modifications as the part is being printed to form composites. These composite filaments can be divided into continuous fiber and discontinuous fiber filaments.

• In continuous fiber systems, a fiber (carbon fiber is commonly used) is coated with a polymer as the part is being printed. Parts printed using these techniques show very high in the direction parallel to the fiber orientation. But it is seen that the out-of-plane strength for these parts remains almost equivalent to that of those printed without the fibers. Thus, this largely limits the use of such filaments in end use applications. Discontinuous fibers have particles in a polymer matrix, these filaments show varying mechanical properties based on the amount of fiber material added to the filament.

• Different papers have also studied an innovative technique of using polymer blend filaments. Additives are added to the polymer to influence its properties like molecular weight, which in turn influence the mechanical properties of the overall parts. This technique has shown a lot of promise and needs to be further studied due to its capability to tweak properties based on additives in the polymer, while maintaining accurate dimensions.

Post-Process Methods

• The review of different works showed that most post processing techniques involve either chemical treatment or exposing the part to an energy source after the part has been printed.

• The chemical treatments are generally used to improve surface finish, and studies have shown that they have a detrimental effect of the mechanical properties of the fabricated parts.

• Some innovative techniques like printing in vacuum or printing in a nitrogen gas chamber have shown to have some positive influence on the mechanical properties. Exposing the parts

printed with Cu fiber PLA composite to a laser is another technique that shows improvement in strength of parts.

• But it has been seen that the most significant post-process techniques involve annealing of the parts. Multiple studies have shown that annealed parts show more than double the tensile strength and fracture toughness of the as built parts. Annealing also increases the ductility of the parts. But a serious drawback of post-process annealing is that it leads to major geometric distortions, thus defeating the purpose of using FFF to fabricate complex parts.

• It should be noted that the cooling rate after annealing affects the ductility of parts printed using PLA. Quenching of the parts after annealing leads to more ductile parts as compared to those that undergo slow cooling.

• This drawback has been addressed exposing parts printed with a dual thermoplastic filament (PC core and ABS shell) to annealing. This technique shows lots of promise as it not only improves the mechanical properties of the parts but also negates the geometric distortion. The only limitation of the process is the process to obtain the dual thermoplastic filament is time consuming and cannot provide the material on a larger scale.

Thus, it can be seen that multiple techniques have been employed to improve the strength of FFF parts, but no single method has provided a final, geometrically accurate, cost- effective and efficient solution to the problem. Though most techniques provide improvement in mechanical properties it should be noted that these techniques have only been applied to simple test specimen with uniaxial loading conditions and not final use parts that are exposed to a much more complex loading condition. Further study also needs to be done on minimizing the geometric distortions

while maintaining the ability to print stronger parts. This review provides important insight to the readers that would allow them to utilize components of each sections mentioned in the review and help them to come up with a recipe that reduces the anisotropy while fabricating geometrically accurate and complex parts.

Chapter 3 Methodology

Process Improvement

From the literature survey it has been seen that the complex temperature distribution around the deposited polymer melt combined with heat transfer between adjacent filaments determines the quality of bond. Furthermore, work has been done on different post and in-situ processes to accentuate the neck growth in FFF parts. Previous work on post-process thermal annealing has shown to increase the inter-laminar bonding by heating the part well beyond its glass transition temperature resulting in significant increase in the mechanical strength of the parts. This method does lead to a substantial increase in strength, but the geometric accuracy of the part is compromised. Also, applying a post -process thermal load increases the total build time of the final part. In-situ approaches have been studied which provide an external heating source to facilitate inter-laminar bonding and these methods have shown great promise. Microwave heating has been used to raise the local temperature during the fabrication of FFF parts. In another study, a complex setup of different optics, mirrors, and a near- infrared laser beam was used to focus the beam on the part to locally raise the temperature before depositing the polymer melt. But these approaches utilize complicated, expensive, and additional equipment further complicating the FFF process. Another study was done by Ravoori et al, where a rectangular metal block was attached to the

nozzle assembly to apply an in-situ thermal load and thus increasing the neck growth. This provided a comparatively simple and cost-effective solution to increasing the inter-laminar bonding by in-situ heating. But this work did not analyze the effect of the thickness of the block and the height of the nozzle from the block on the mechanical strength of the parts. Also, previous studies have shown that inter- laminar bonds are the weakest along the out-of-plane or z-direction due to the reduced reptation and neck formation seen when a hot polymer melt is extruded onto a layer that has already cooled down. But in the work done by Ravoori et al, the tensile coupons printed were not oriented with their length along the out-of-plane direction rather they were laid flat onto the bed thus not providing an accurate representation of the neck growth phenomenon between two consecutive layers but rather two adjacent beads. Preliminary studies also showed that using the setup as seen in the work by Ravoori et al inhibits the geometric freedom of the parts as tall or slender parts cannot be printed due to the lack of a cooling mechanism above the block resulting in the filament softening prematurely due to excessive conductive and convective heat transfer upwards by the block causing under or no extrusion of the filament. Thus, designing an entire heater block assembly is desirable that takes these issues into account and provides a solution to the reduced mechanical properties of FFF parts.

In the current work a print head assembly has been designed to apply an in-situ thermal load while the part is being printed as shown in Figure 8. A heater block is designed with a circular block integrated into the heated liquefier. Two factors namely block thickness and nozzle height from block are studied each factor with 3 levels. A design of experiments (DOE) is performed using a two-way full factorial analysis to study and characterize the ultimate tensile strength (UTS), toughness and fracture toughness and obtain a statistical model. Analysis of Variance (ANOVA) is conducted to test the significance of each factor on the increase in UTS), toughness and fracture

42

toughness and find the optimum value from the different combinations. Further an analytic model of the modified heater block with and without the cooling setup is performed to study its utility and effectiveness in printing tall and slender parts and solving the issue faced by the work done by Ravoori et al. Characterization of the change in the cross-sectional area is done to see how the modified heater block assembly affects the geometric accuracy of the parts. Changes in the characteristic long voids seen between adjacent rasters and cross-sectional images were analyzed. This study provides a detailed analysis of the contribution of different factors of the modified heater block assembly and overcomes the challenges faced in previous studies.
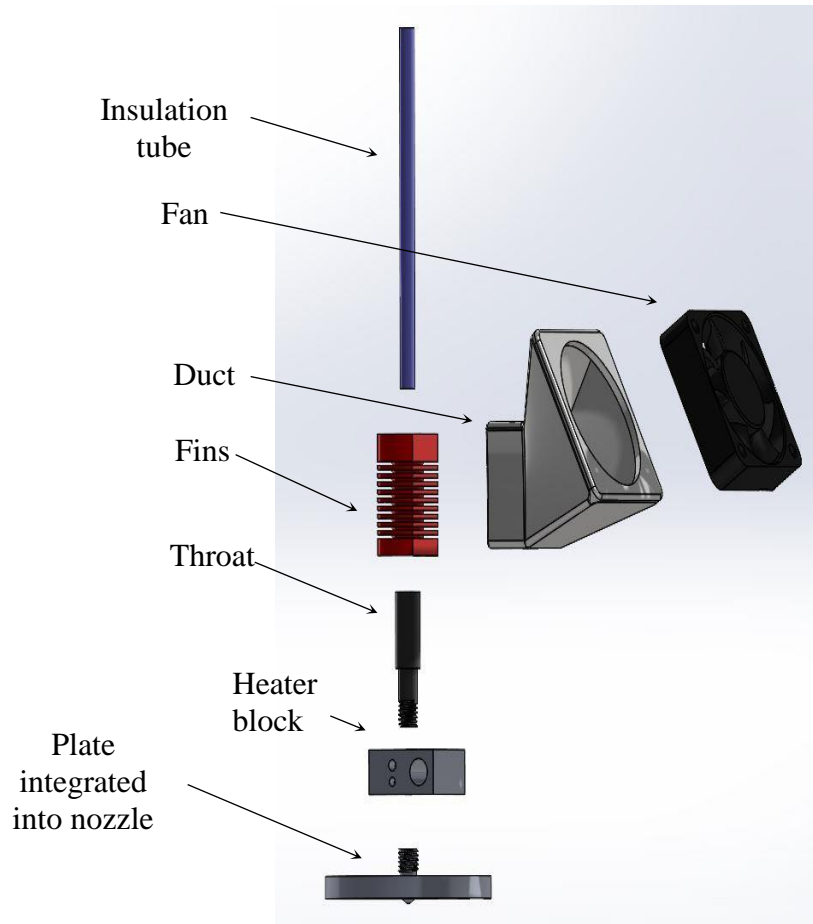
Figure 8. Novel print head assembly

Materials and Testing

For the experiments, parts were printed using Polylactic Acid (PLA) filament (Hatchbox 3D, Pomona, CA, USA) of 1.75 mm diameter. Tensile test coupons (dog ones) were printed using a modified design of the ASTM D638-02a standards as shown in Figure 9 and the compact tension (CT) specimen were printed using ASTM D5045-99 [131]. The test coupons were designed on SOLIDWORKS 2016 (Dassault Systems, Waltham, MA, USA) and converted to G-Code using Simplify3D software. Figure 9 shows the experimental setup consisting of Creality Ender 3 Pro printer with the attached modified heater block assembly. The print and bed temperature were kept at 473 K (200˚C) and 333 K (60˚C) respectively and printed with a 0.4 mm brass nozzle. The infill percentage for the coupons was kept at 100% with no perimeter shells. Previous studies had used print setting which provided parts with a considerably low reference value as compared with those obtained by the current settings leading to an inaccurate and inflated depiction of the factor effects. These print settings were used as they provided the best results in terms of print quality, strength, and reduced print times. The dogbone samples were printed with their longest dimension parallel to the build direction (z-direction). This was done to achieve an accurate representation of the weak inter-laminar bonds between two adjacent layers and therefore provide results for increase in UTS for the weakest inter-laminar bonds. The CT specimen were printed such that the crack plane was parallel to the layers to characterize the interlayer fracture toughness (K_{Ic}) as shown in Figure 9. To print the CT specimen with a pre-cracked zone, a specific procedure was followed. An alarm was inserted in the G-code to indicate that half the number of layers have been printed. Once this alarm went off a fixture was used to insert a Kapton tape which forms the pre-crack in the CT specimen as shown in Figure 9. The infill raster angle was kept at 0 to obtain maximum inter-laminar bond area.

The circular aluminum heater block discs were 50 mm in radius and had 3 levels of thickness: 2mm, 5mm and 10 mm. The nozzle height from the block was adjusted to 3 levels: 1mm, 1.5mm and 2mm. To ensure consistency the printer was placed in an enclosed room with desiccant to avoid humidity issues. A cooling fan with a duct was provided for localized cooling above the heated liquefier region as seen in the Figure 10. In previous studies the tensile test coupons are printed lying flat on the bed (longest dimension of specimen along the bed plane), an absence of a localized cooling mechanisms in these studies puts a limitation on printing tall and slender parts along the out-of-plane or z-direction. Localized cooling is necessary because preliminary tests showed that the heat generated due to the block travels upwards via conduction and convection leading to softening of the filament in the upper sections of the extrusion chamber causing print failure after printing some layers as seen in the Figure 11.
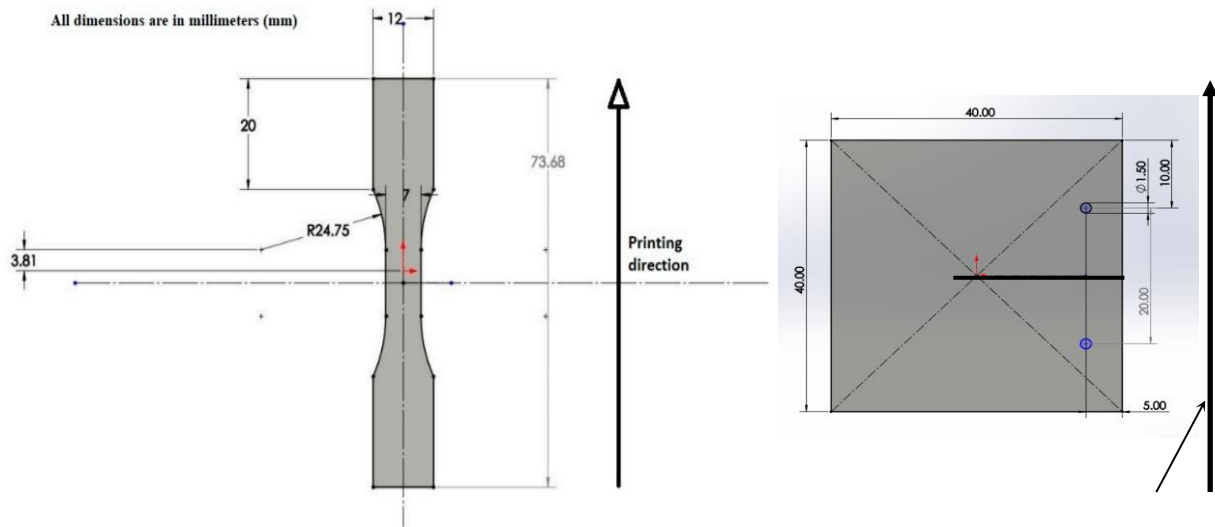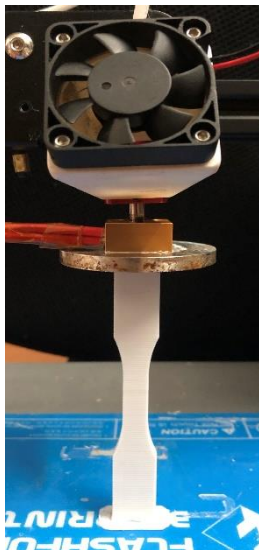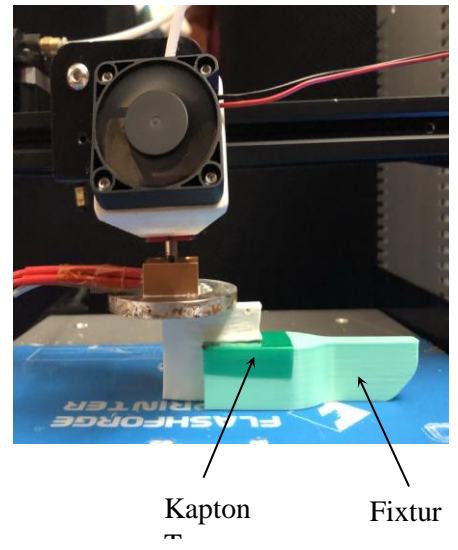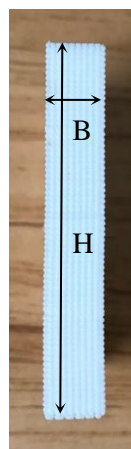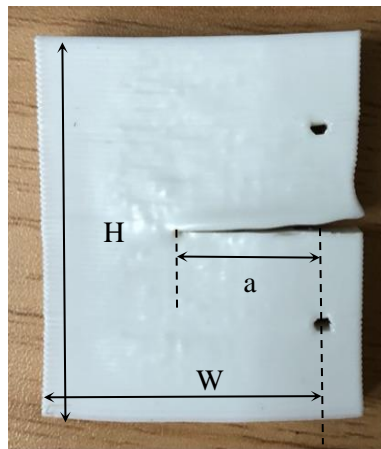
Figure 9. Dimensions and Fabrication of Tensile and CT specimen

Standard hot ends provide fans to cool the part being printed as well as the upper sections of the extrusion chamber but using these attachments result in the heater block to be continuously cooled leading to extended wait times in heating up the heater block and thermal runaway errors in the printer. Thus, using the customized cooling mechanism solves the issues discussed. To study the effect of the cooling mechanism on temperature distribution in the assembly, a transient state thermal analysis is run on it with and without fan as shown in Figure 12. For the part without the fan, a convective boundary condition was applied over the fins with a heat transfer coefficient of 10 $W/m^{2}K^{-1}$ was chosen for which stands true with the ambient conditions for natural convection [93]. Whereas for the assembly with a 40 mm fan, a convective boundary condition with heat transfer coefficient of 100 $W/m^{2}K^{-1}$ was applied over the fins section of the assembly [132]. The simulations show that the temperature in the throat is much higher for the assembly without a fan whereas the temperature in the throat falls below the glass transition temperature of PLA when a fan is used. FFF systems require the filament to maintain its structural integrity before entering the heated liquefier to act as a piston and push out the polymer melt through the nozzle, which is achieved by using the cooling mechanism. Also, by localizing the cooling area, the specimen and the block can be maintained at a higher temperature resulting in better welding between layers. Thus, a localized cooling mechanism not only solves the issue of printing slender parts oriented in the z-direction but also allows for better welding between adjacent layers.

Teflon tube

Forced cooling section

Fins

Throat

Heater block

Thermocouple
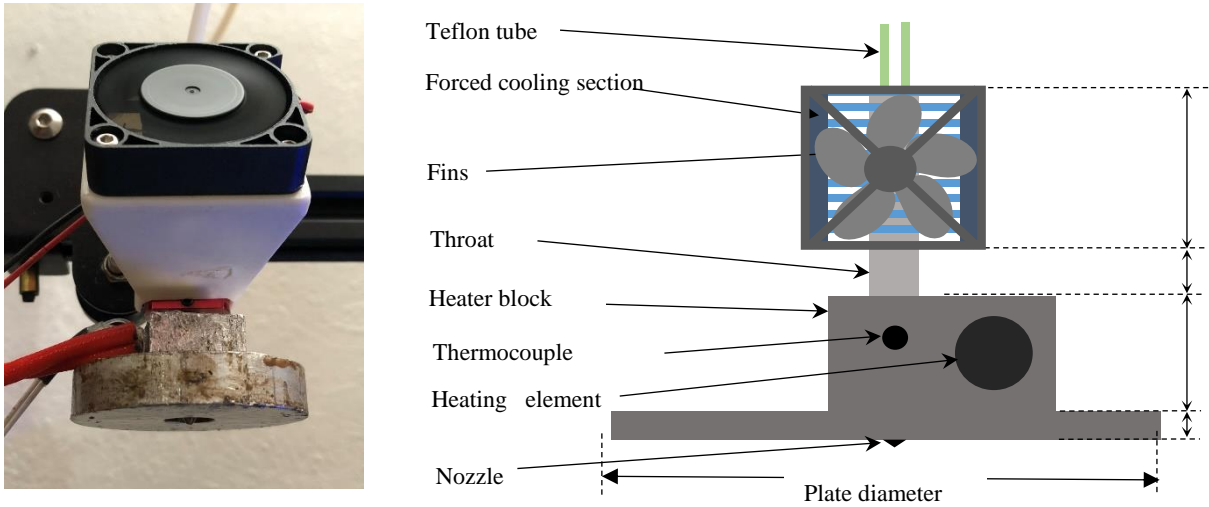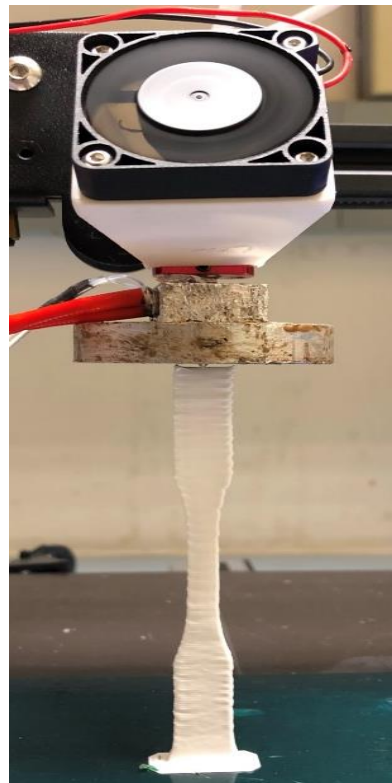
Heating element

Nozzle

Plate diameter

Figure 10. Cooling mechanism for localized cooling above the heated liquefier

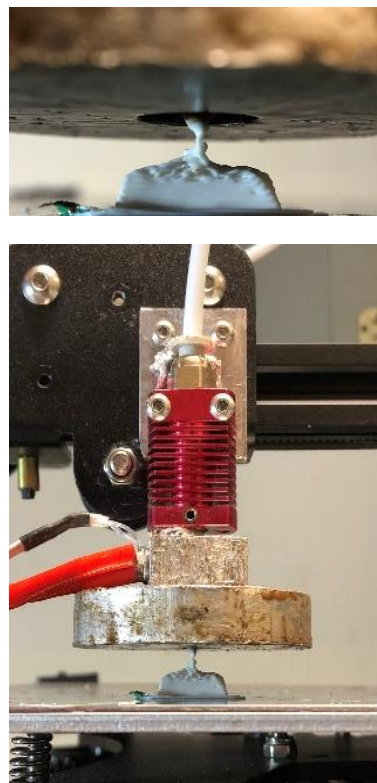**Successful print with cooling mechanism**   **Print failure without cooling**

Figure 11. Issues due softening of the filament due to absence of cooling mechanism

Each part was printed separately to avoid compounding error and provide replications for the different factor levels. Both the tensile and CT parts were then tested under tensile loading using a Shimadzu Tensile Testing machine. To apply the tensile load a displacement control of 5mm/s was applied on the specimens using a 10 kN Load cell. The data obtained from the tensile tests was in the form of Load versus Stroke which was converted to stress versus strain by dividing by the appropriate values of area and length, respectively. The maximum value of stress of each specimen was considered as the ultimate tensile stress whereas the area under the curve was calculated to obtain the toughness (strain energy) of the parts. For calculating the K_{Ic} of the CT specimen, the ASTM 5045-99 was followed. A linear elastic fracture under plain strain condition was assumed to occur in the CT specimen. The linear elastic assumption was confirmed using the Equations 4-6, whereas the dimensions of the CT specimen accomplish the plane strain condition. A 95% secant offset method is used as described in ASTM 5045 to accurately find the maximum load P_Q and P_{max} shown in Equation 4. Equation 4 ensures that the non-linearity in the load-displacement curve is related to the crack initiation and not the growth of a large plastic zone. Equations 5 and 6 ensure that the specimen is in plane strain condition while avoiding excessive plasticity in the ligaments of the specimen.

$$\frac{P_{max}}{P_Q} < 1.1 \tag{4}$$

$$0.45 < a_o/W < 0.55 \tag{5}$$

$$B, a_o, (W\text{-}a_o) < 2.5 \left(\frac{K_Q}{\sigma_y}\right)^2 \tag{6}$$

Where, P_{max} = Maximum load before failure, P_Q = Trial critical load, a_o = Initial crack length,

B = Thickness, W = Width, H = Height, K_Q = Trial Fracture Toughness, and σ_y = Yield strength.

The yield strength is calculated from the tensile specimen printed for the different treatment combinations and these are used to calculate the K_{Ic}. The K_{Ic} values are calculated using the Equations 7 and 8 obtained from ASTM 5045-99, where $f\left(\frac{a_O}{W}\right)$ is the geometric function of the CT specimen.

$$f\left(\frac{a_O}{W}\right) = \frac{\left(2+\frac{a_O}{W}\right)}{\left(1-\frac{a_O}{W}\right)^{\frac{3}{2}}}\left[0.886 + 4.64\left(\frac{a_O}{W}\right) - 13.32\left(\frac{a_O}{W}\right)^2 + 14.72\left(\frac{a_O}{W}\right)^3 + 5.60\left(\frac{a_O}{W}\right)^4\right] \tag{7}$$

$$K_{Ic} = \frac{F_c}{B\sqrt{W}}f\left(\frac{a_O}{W}\right) \tag{8}$$

The increase in fracture toughness is obtained by subtracting the value of the average K_{Ic} of the five reference specimen from the K_{Ic} of the specimen printed for the different treatment combinations.

The stiffness of the parts was calculated in accordance with the ASTM Standard D638 by providing appropriate toe compensation and assuming Hookean behavior in the lower sections of the Stress-Strain curve.
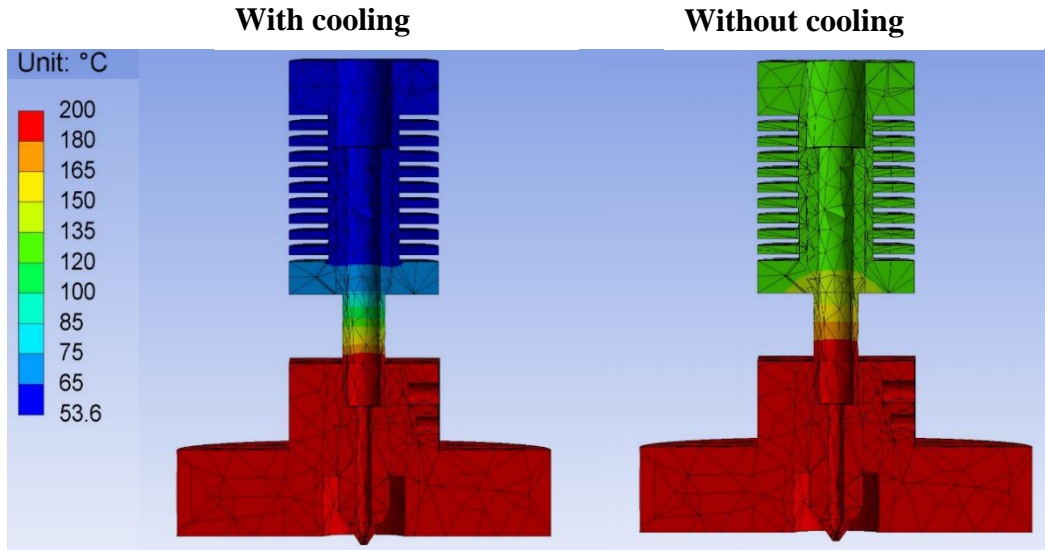
With cooling   **Without cooling**

Figure 12. Temperature distribution in heater block assembly with and without cooling mechanism

The experiments and analysis were conducted using a full factor DOE for three response variables: Increase in Ultimate Tensile Stress, Increase in Toughness and Increase in Fracture Toughness. To obtain a comprehensive statistical model and the factor level effects, 3 levels of nozzle height and plate thickness were chosen as summarized in Table 4. The two-way full factorial DOE runs for each combination of factors mentioned in Table 4. Thus, the experimental design included a total of 9 treatment combinations with 5 replications for each treatment. To avoid systematic biases the treatments were performed in a randomized order. Each part was printed separately on the Creality Ender 3 with each tensile specimen taking 68 minutes and CT specimen taking 95 minutes to print. After each print, the brim (skirt) around the tensile specimen was carefully removed with no further post-processing on the specimen. After completing all the treatments, the parts were tested under a tensile load to obtain the ultimate tensile strength, toughness and fracture toughness. The reference values were obtained by printing 5 specimens with the same G-code as the treatments, using the stock heater block assembly as provided with the Creality Ender 3. The increase in

tensile strength, toughness and fracture toughness is obtained by subtracting the values obtained for the control specimens with those of the treatment combinations. Values of stress, strain toughness and fracture toughness were calculated using MATLAB and the statistical analysis was performed using SAS (SAS Institute Inc; Cary, NC).

Table 4. Nozzle height and Plate Thickness levels for the design of experiments.

Levels	Nozzle Height (mm)	Plate Thickness (mm)
1	1	2
2	1.5	5
3	2	10

Chapter 4 Results

For the heater block assembly, a finite volume simulation model has been studied to analyze the temperature field around the block during motion. In the following discussion the DOE assumptions have been verified and the appropriate statistical model along with the ANOVA analysis has been stated.

Finite Volume simulation model

The temperature of the previously deposited layers is affected by 2 heat sources: the jot dispensed polymer melt and the block. A finite volume simulation was run to study the effect of the block combined with the nozzle on the previously deposited layers. The simulations are carried out on ANSYS Fluent. The transient state simulation is performed on the block motion using dynamic mesh motion. Linear motion in the x-axis is provided to the block and a new mesh is formed at each timestep as the block moves in the ambient air volume.
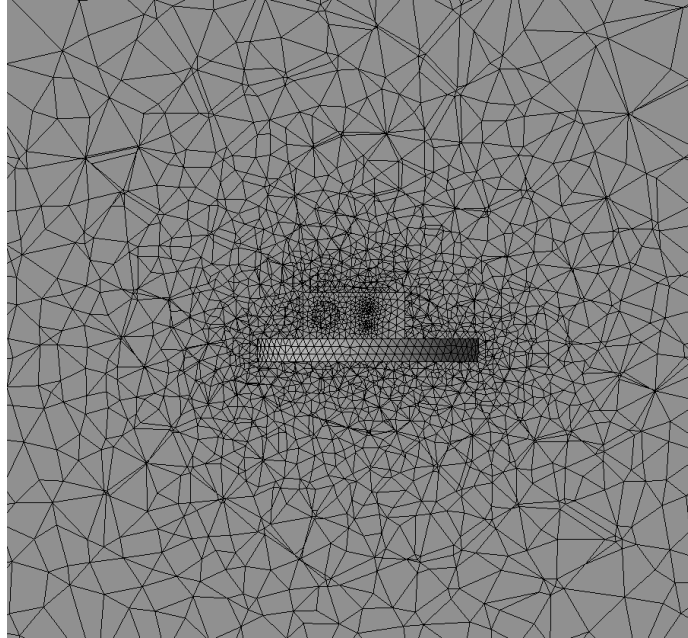
Figure 13. Meshing of the block enclosed in air.

A Computer Aided Design (CAD) model of the block is built using Solidworks. In the model the heater block is maintained at 473 K while keeping the ambient air at 300 K. Natural convection boundary conditions are applied to the surface of the block. The block is defined as a rigid body and motion is allocated to it using a user defined function (UDF). The speed of the block is maintained at 60 mm/s which is used as the default print speed in most printers. The time step is kept at 0.01s which is much smaller than the local cell size, this prevents negative cell volume and cell degeneration issues. With each time step local remeshing is done for cells significantly affected by the rigid body motion of the block. This is done to account for issues like cell size exceeding minimum or maximum size criteria and excessive skewness. Figure 13 shows the

meshing of one of the blocks. A sizing mesh method is applied around the block for a finer mesh and accurate heat transfer results.

Raw increase in strength, strain energy and Fracture toughness due to nozzle height variation from the block

a) Raw increase in ultimate tensile strength

Figure 14 shows an increase in ultimate tensile strength with respect to the nozzle height. From Figure 14 we see that as nozzle height increase from 1mm to 2mm a fall in the average ultimate tensile is obtained. As the nozzle height approaches 2mm, the top layer is exposed to a lower temperature field as compared to that when the nozzle height is kept at 1mm. This can be seen from the contour plots obtained from the simulation models in Figure 15. Figure 16 shows the temperature profile at a predefined plane 0.3mm away from the nozzle. Figure 16 shows the temperature variation with time of a point on the defined plane as the block moves over it. It is seen from Figure 16 that as nozzle height increases from 1mm to 2mm the temperature on this plane falls by approximately 10 K. But for different plate thicknesses, the temperature profile remains somewhat similar at the defined plane as seen from contour plots in Figure 15. This difference in temperature profiles with changes in nozzle height affects the bonding between the layer being deposited and the previous layer. Previous studies have shown that when the temperature of the previous layer is maintained at a higher level an increase in the strength is obtained due to better neck formation and reptation. This holds true for the current study; we see that the average increase in the ultimate tensile strength of the parts falls from 23.3 MPa to 16.2 MPa as we increase nozzle height from 1mm to 2mm.
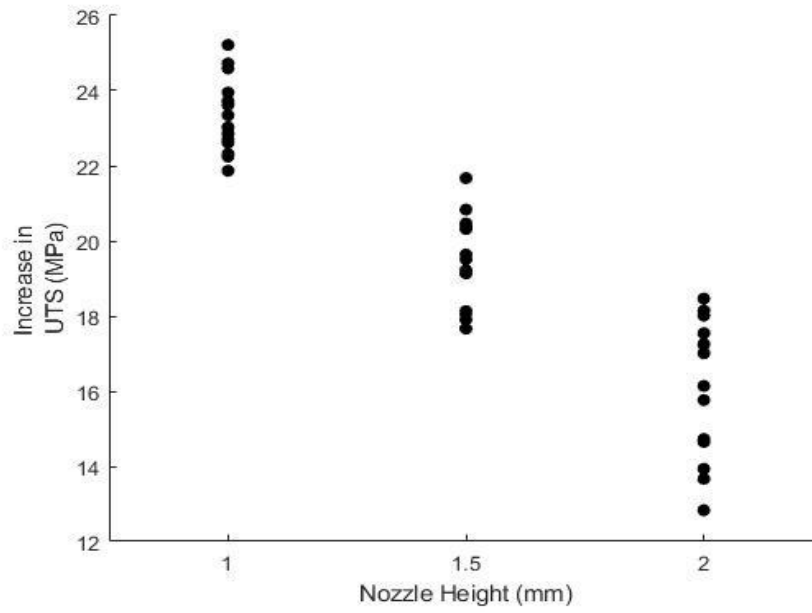
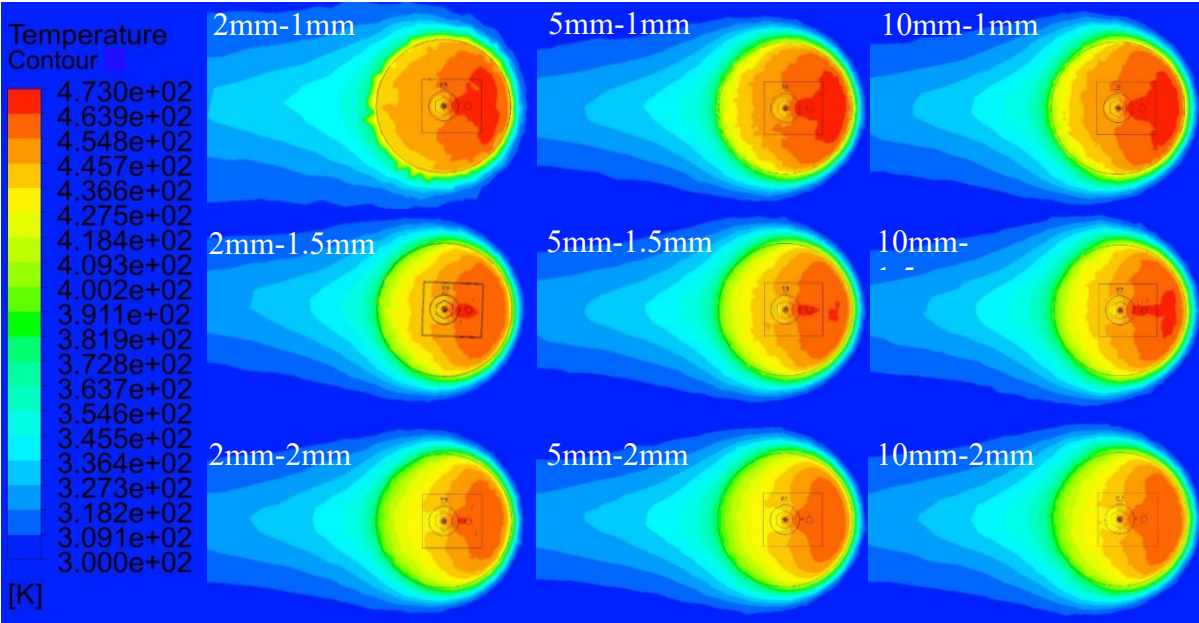Figure 14. Plot showing Raw increase in strength with nozzle height

Figure 15. Simulation model showing temperature contours on a plane 0.3 mm away from the
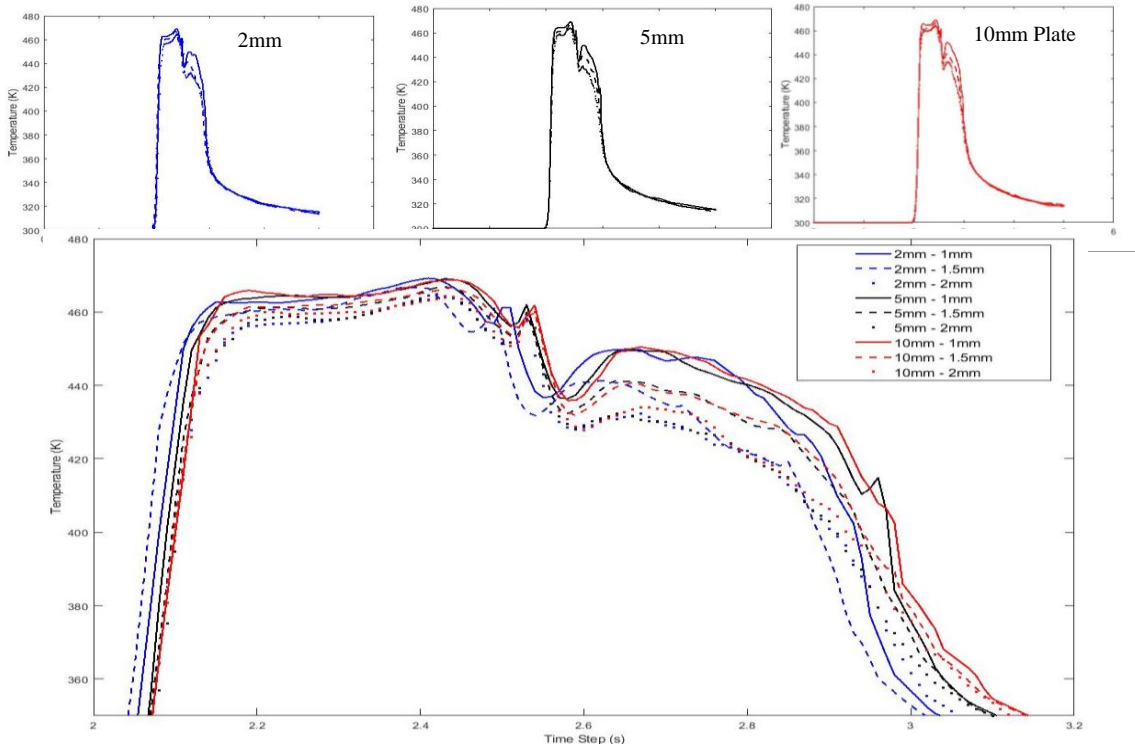
nozzle.

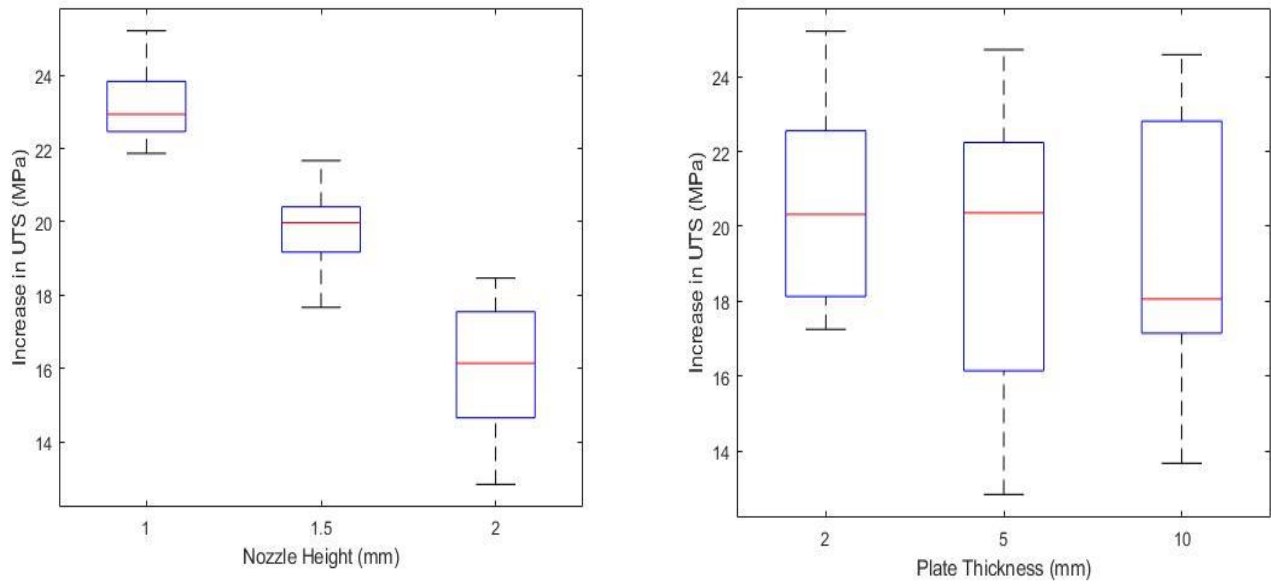Figure 16. Temperature vs Time Step plots.

Figure 17. Plot showing Raw increase in strength with Plate thickness.

However, on studying raw increase in strength with plate thickness as shown in Figure 17, no trend or notable difference is seen. The average increase in strength is seen to be maximum for the 2mm followed by 10mm and 5mm plate. The simulation models show that when the nozzle height is kept constant for different plate thickness, the top layer is exposed to the same maximum temperature as seen in Figure 15. This gives rise to a necking and bond formation process which is similar across different plate thicknesses, thus showing no or little difference for increase in average ultimate tensile strength between different plate thicknesses. When the variances from Boxplots in Figure 18 are compared, it is seen that the nozzle height has a dominant effect on the increase in ultimate tensile strength of the parts as compared to the plate thickness. A general upward trend is noticed as the nozzle height is varied from 2mm to 1mm. No such trend can be concluded for the effect of plate thickness on the increase in UTS of the parts.

Figure 18: Boxplot showing variance in distribution of increase in UTS for different nozzle

heights and plate thickness.

b) Raw increase in Toughness (Strain Energy)

From Figure 19, it is seen that effect of nozzle height on toughness is similar to its effect on UTS. As the nozzle height moves away from 1mm to 2mm, a consistent fall in the strain energy is seen. The average increase in toughness of the parts falls by more than 50 % (2159.06 KPa to 1029.35 KPa) as the nozzle height increases from 1mm to 2mm. Increase in toughness can be correlated to the reptation across the interfaces which is influenced by the exposure temperature and time of the layers. For a nozzle height of 1mm the top layers are exposed to a much higher value of temperature as compared to the nozzle height of 2mm, thus leading to a significant fall in toughness with increase in nozzle height. Simulation models shown in Figure 20 help us understand the temperature distribution around the plate. If we consider a vertical line under the nozzle as shown in Figure 21, as the distance from the nozzle increases the temperature falls. This fall in temperature along a line starting 0.3 mm (layer height) below the nozzle to

58

15 mm has been plotted in the Figure 21. For different nozzle heights, the temperature field changes after 7 mm distance from the nozzle as seen in the Figure 21 and this is confirmed from the contour plots. This shows that for smaller nozzle heights the layers remain at a higher temperature for a longer time as compared to those with larger nozzle heights. Thus, it allows for greater reptation and intermingling of the polymer chain leading to enhanced toughness.
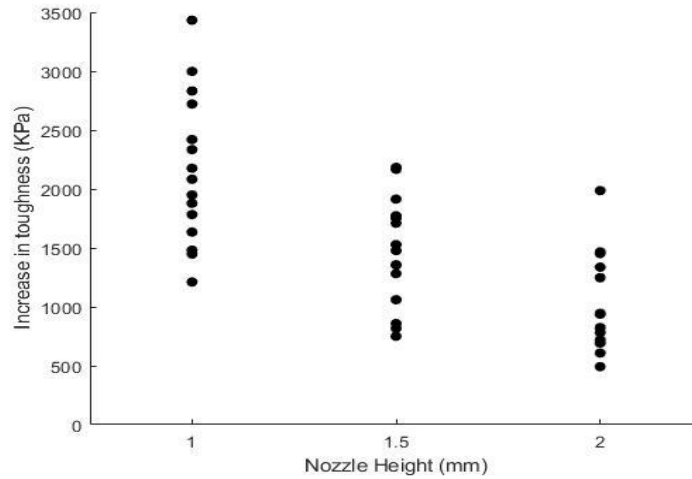

Figure 19. Plot showing Raw increase in Toughness with nozzle height.

Figure 19 shows the effect of plate thickness on the raw increase in toughness. A general upward trend in the increase in average toughness is noticed as the plate becomes thicker. As the plate thickness increases from 2mm to 10 mm the increase in average toughness goes up from 1225.05 KPa to 1742.73 KPa. This can be attributed to the fact that for a larger plate, the layers are exposed to a higher value of temperature for a longer time duration. Simulation models from Figure 20 and 21 shows that this hypothesis holds true.
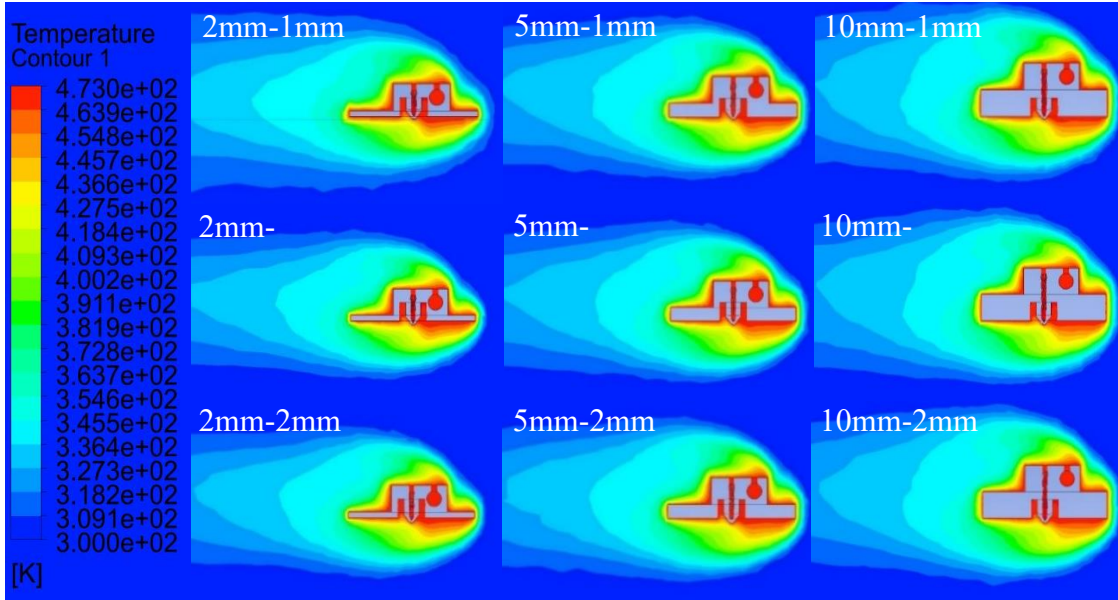
Figure 20. Simulation model showing temperature contours around the heater block
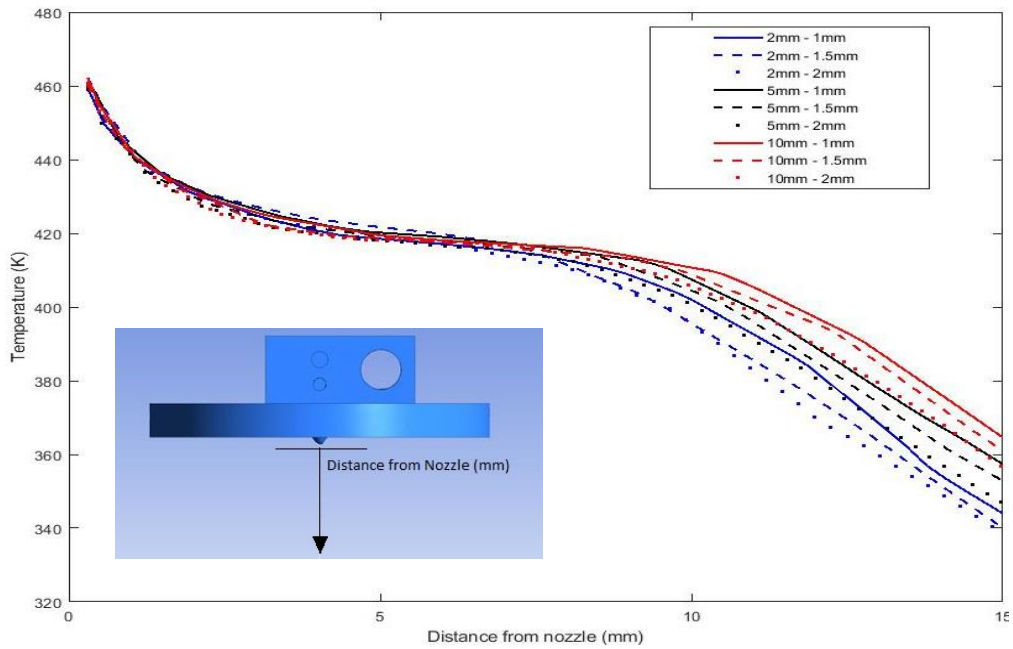

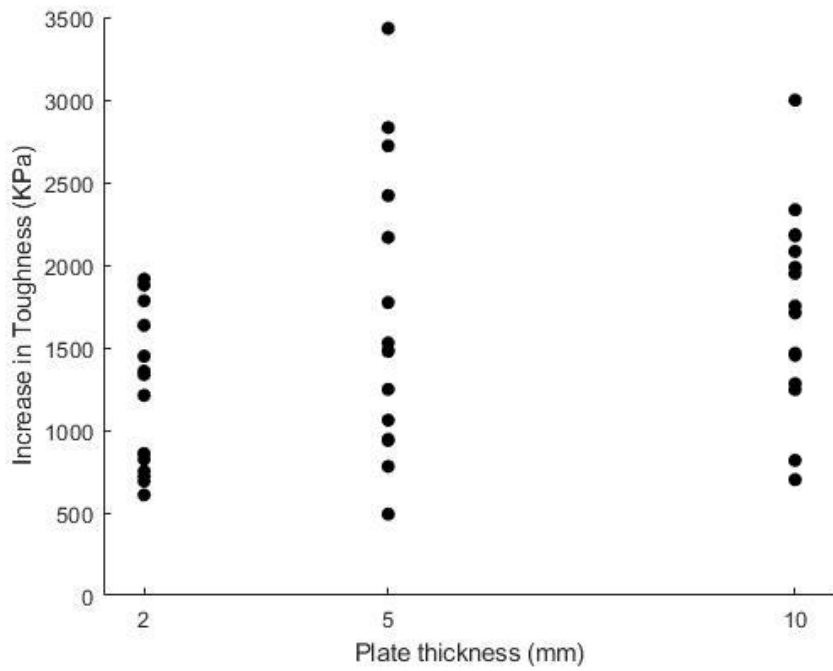Figure 21. Temperature variation as we move away from the nozzle

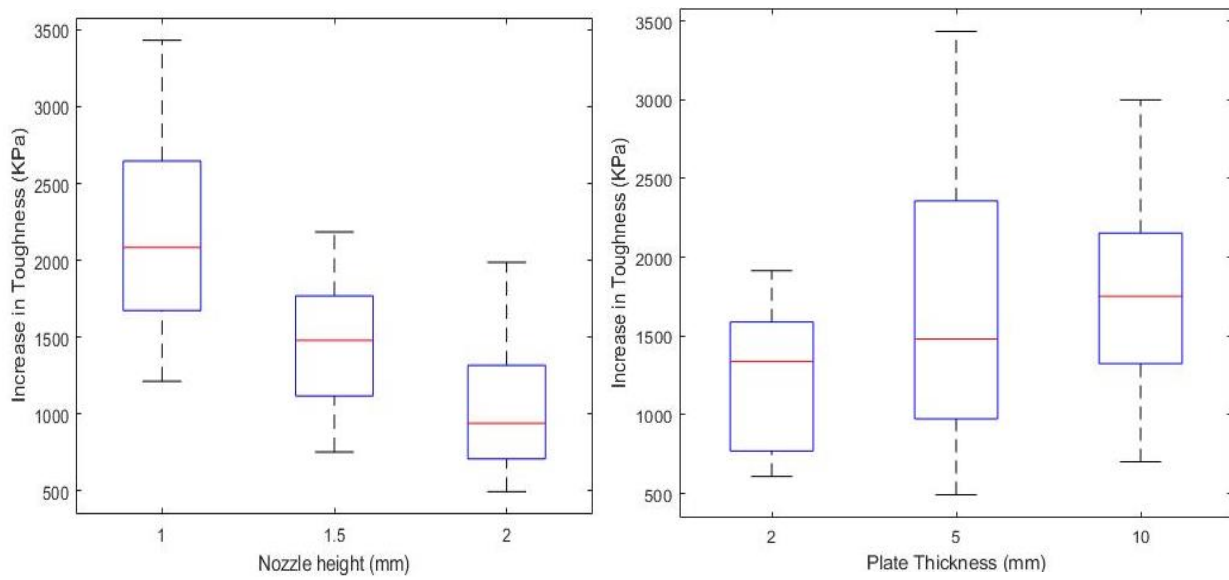Figure 22. Plot showing Raw increase in Toughness with plate thickness

Figure 23: Boxplot showing variance in distribution of increase in Toughness for different nozzle

heights and plate thickness.

61

Figure 18 shows that for 10 mm thick plate the temperature at a distance of 10 mm from the nozzle the is around 420 K whereas for the 2 mm thick plate at the same distance the temperature is 410 K. Also, from the plots it can be studied that the temperature gradient is much more gradual for the 10 mm plate whereas a steeper fall is seen for the 2mm plate.

The boxplots in Figure 23 show that increase in toughness has a larger spread for plate thickness as compared to nozzle height showing a dominant effect of the nozzle height. Also, a positive correlation is seen between increase in plate thickness with the increase in toughness whereas a negative correlation between increase in nozzle height and increase in toughness is seen.

c) Raw in Increase in Fracture toughness (K_{Ic})

From Figure 24, it is noticed that with an increase in nozzle height a negative trend in average increase in fracture toughness is seen showing a presence of main effects due to the nozzle height. As nozzle height increases from 1mm to 2 mm the average increase in fracture toughness falls from 22 MPa$\sqrt{mm}$ to 5 MPa$\sqrt{mm}$. This fall can be explained using simulations in Figure 21 and 20. Figure 21 shows that for 1mm nozzle heights the top surface of the printed specimen is at a much higher temperature as compared to other nozzle heights, thus leading to better inter layer bond formations and improved fracture toughness.
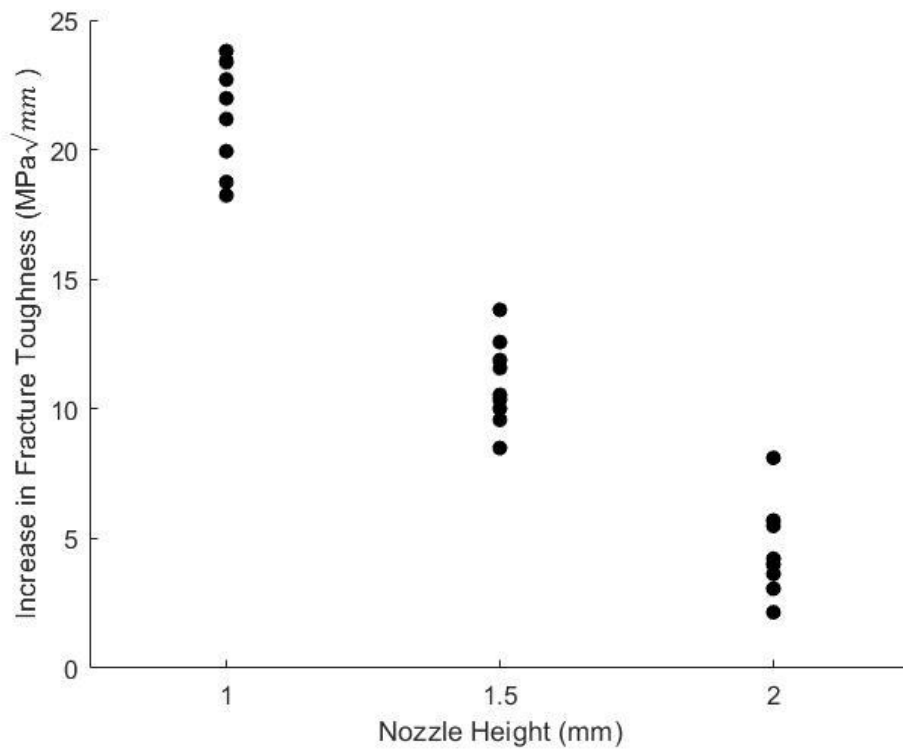

Figure 24. Plot showing Raw increase in Fracture Toughness with nozzle height.
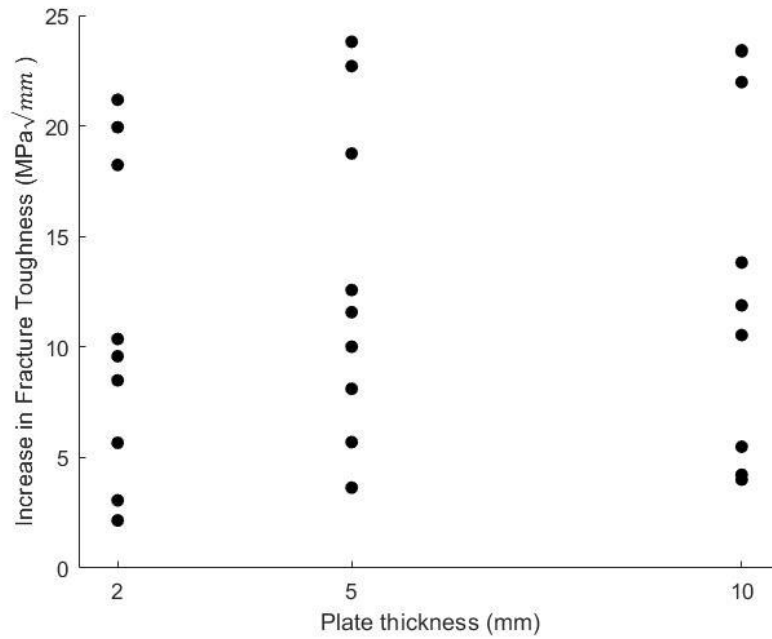
Figure 25. Plot showing Raw increase in Fracture Toughness with plate thickness

From Figure 25, it is seen that for an increase in plate thickness a slight positive trend is seen in the average increase in fracture toughness. It is seen that the fracture toughness increases from the 2mm plate thickness to the 5mm plate thickness but for the plate thickness of 10 mm it remains almost similar to that of the 5mm plate thickness. From the simulations it has been seen that larger plate thicknesses keep a greater number of layers heated above the glass transition temperature for a longer period of time. Theoretically this has been shown to allow for better intermingling and reptation of polymer molecules leading to improved fracture toughness of the parts.

Figure 26 shows the box plots for both nozzle height and plate thickness. On studying the box plots for both factors, it is seen that the nozzle height has much smaller spread as compared to the plate thickness showing a dominant effect of nozzle height.
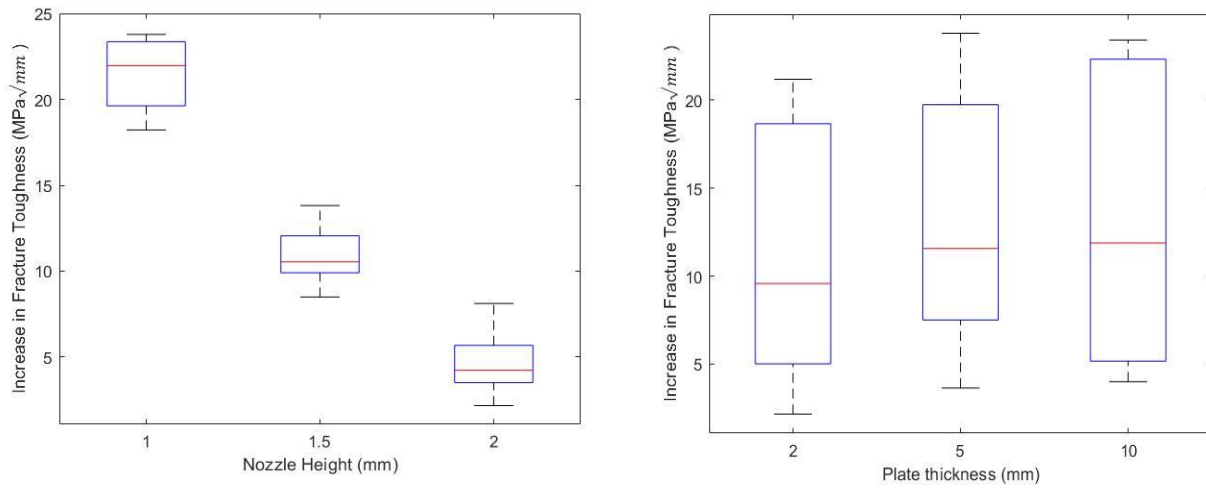
Figure 26: Boxplot showing variance in distribution of increase in Fracture Toughness for different nozzle heights and plate thickness.

Two-way fixed effects model and assumptions verification.

In the current study for all three response variables, the two-factor full interaction model is given as,

$$Y_{ijt} = \mu_{..} + \alpha_i + \beta_j + (\alpha\beta)_{ij} + \varepsilon_{ijt} \tag{7}$$
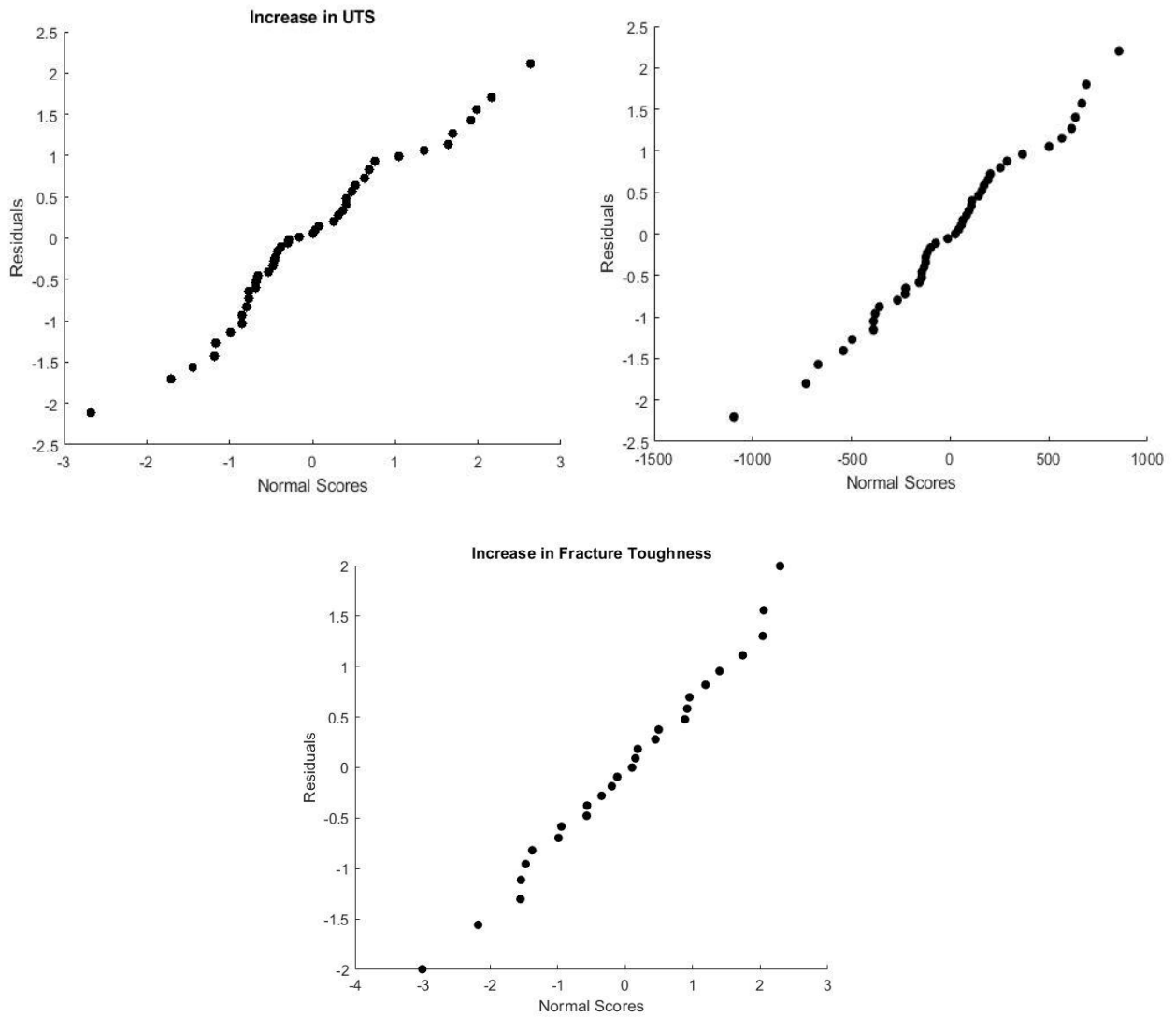

Figure 27. Normal Probability Plot for response variables.

Here were assume that the model has unknown fixed effects subjected to the following restrictions:

restrictions $\sum_i (\alpha)_i = 0$, $\sum_j (\beta)_j = 0$, $\sum_i (\alpha\beta)_{ij} = 0$ and $\sum_j (\alpha\beta)_{ij} = 0$. Also, it is assumed that the error term in the ANOVA model, ε_{ijt} is normally distributed with constant variance and mutually independent errors. The assumption of normally distributed residuals is done by visually inspecting the Normal Probability Plot (NPP) for all responses as shown in Figure 27. It is seen that all plots have some sampling variations but lack of any heavy tails and no serious departures from normality. Therefore, the assumption of normality is satisfied for all three response variables [133]. As normality is satisfied a transformation does not need to be applied to the data and we can continue with the linear model chosen in Equation 7.

Now the assumption of constant variance is checked. To check for this assumption the residuals are plotted as a function of fitted values (estimated means, $\hat{y}$) as shown in Figure 28. From Figure 28 for all three response variables (Increase in UTS, Increase in toughness and Increase in Fracture toughness) there are no collocated residuals, and the scatter of points are randomly distributed with somewhat equal spread. Therefore, the assumption of constant variance can be said to be satisfied.
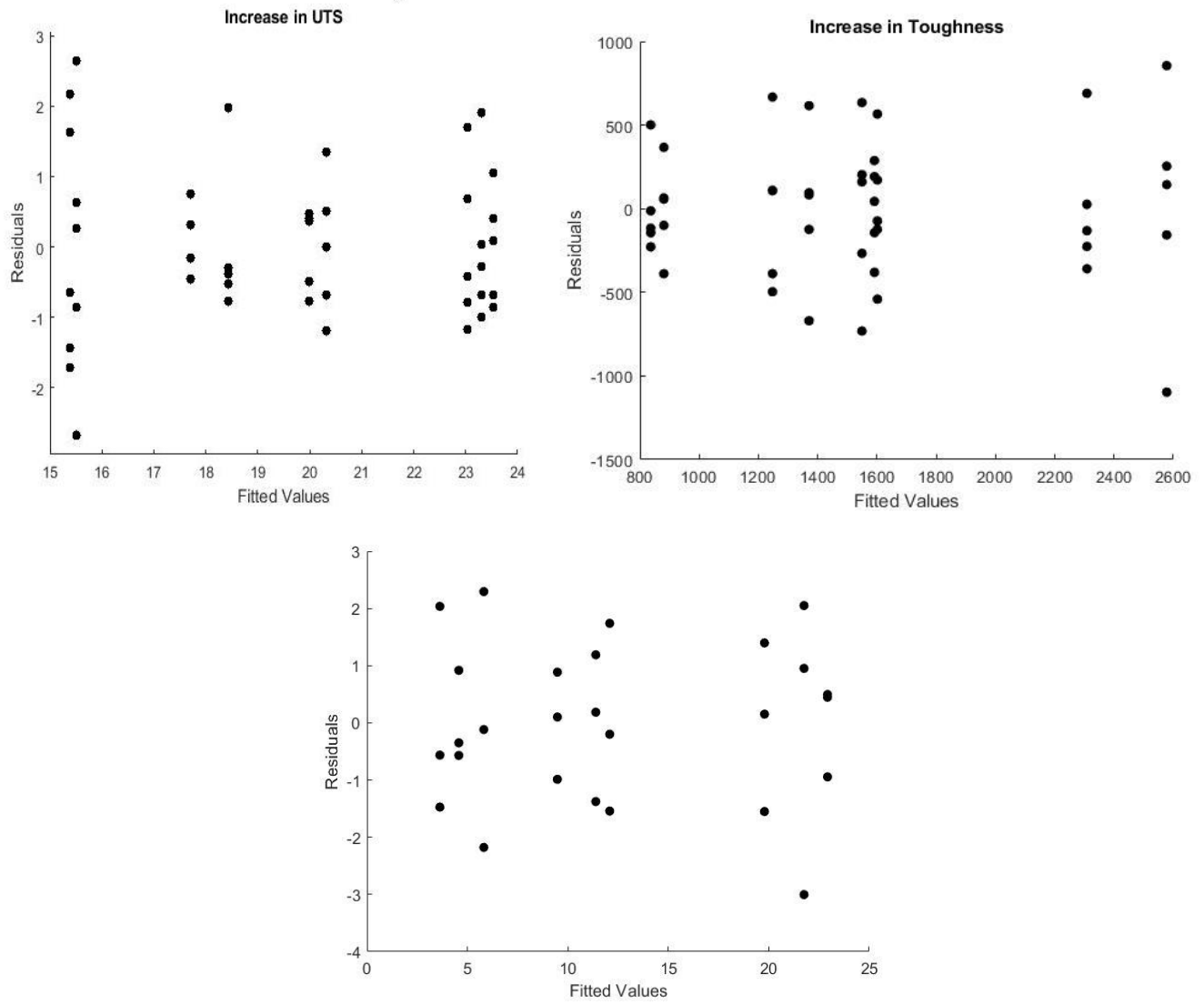
Figure 28. Residuals vs. Fitted values plot

ANOVA and Factor interactions

a) Increase in UTS

From the interaction plots shown in Figure 29, 3 distinct lines are seen which shows that the main effects for the nozzle heights are present. With an increase in nozzle height the average increase in UTS falls thus indicating that for 1 mm nozzle height we obtain maximum increase in UTS. A fall in the average increase in UTS is seen for 2mm plate thickness to 5mm plate thickness for 2mm nozzle height, but this can be attributed to the presence of sampling variability. The 3 distinct lines show a slight fall in average increase in UTS for the 5mm plate thickness plate, but the overall trend is to remain constant with zero slope thus indicating the absence of main effects due to plate thickness which can be further verified from the ANOVA results shown in Table 5.

Table 5. ANOVA for the Increase in UTS

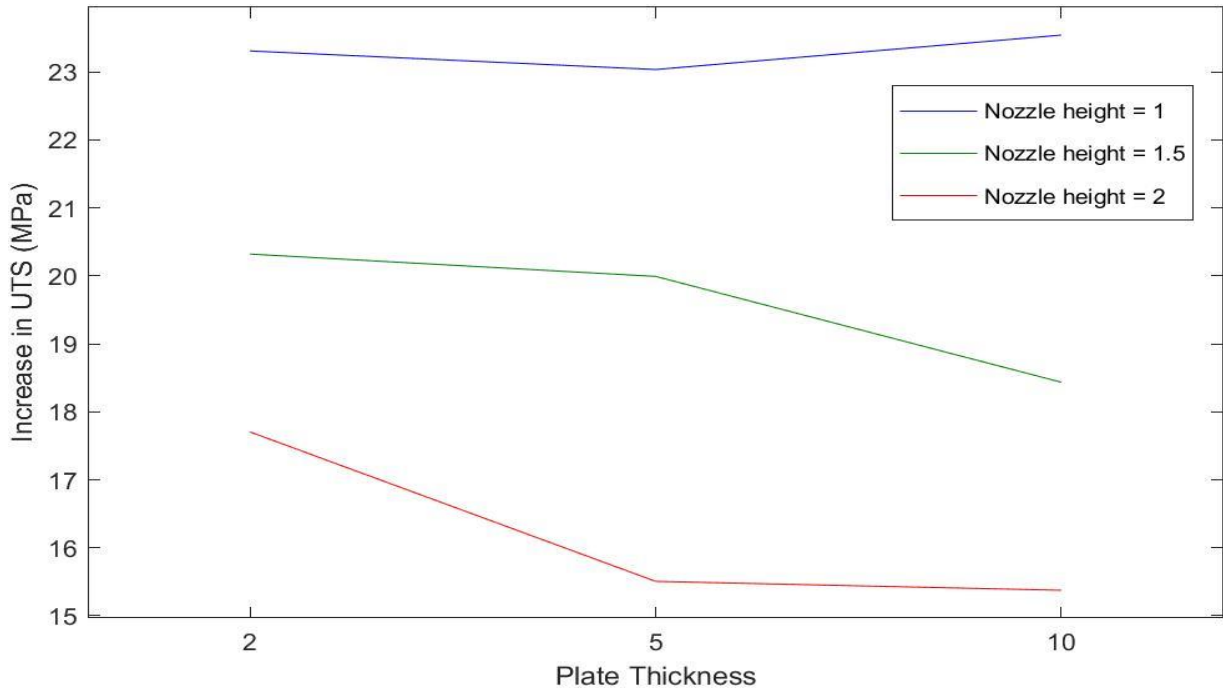| Source	Degrees of Freedom	Type III Sums of Squares	Mean Square	F value	Pr > F
Nozzle Height (h)	2	378.24	189.12	129.17	<.0001
Plate thickness (t)	2	13.93	6.97	4.76	0.0147
h × t	4	13.97	3.49	2.38	0.0694
Error	36	52.71	1.46		
Corrected Total	44	458.85			

Figure 29. Interaction plot for increase in UTS.

From the ANOVA results we see the breakdown of the variability (sums of squares) of the response variable, increase in UTS. Nozzle height has the maximum contribution to the variability, and 89% of the variability in the response can be explained by the full interaction model. From the ANOVA results we see that, for the interaction effects, the p-value (0.0694) > 0.01 (confidence level of 99%). Thus, it can be concluded that the interaction effects are negligible. Due to the absence of interaction effects, we now check for the main effects due to the plate thickness and nozzle height. The p-value for the plate thickness (t) (0.0147) > 0.01 (confidence level of 99%), thus indicating the absence of main effects due to plate thickness at a 0.01 significance level, but for a 0.05 significance level the main effects due to plate thickness are present. The absence of

interaction effects on the increase in UTS shows that for future work the appropriate model is the additive model,

$$Y_{ijt} = \mu_{..} + \alpha_i + \beta_j + \varepsilon_{ijt} ,$$ (5)

that has the assumptions that $\sum_i (\alpha)_i = 0$ and $\sum_j (\beta)_j = 0$, where α_i = main effects due to nozzle height, $\mu_{..}$ = overall mean for all treatments and ε_{ijt} = error term.

b) Increase in Toughness

From the interaction plot for increase in toughness shown in Figure 30, we see that there are 3 distinct lines present for corresponding to the nozzle heights, indicating the presence of main effects due to the nozzle heights. Here we see that as nozzle height increases there is a drastic fall in the average increase in toughness of the specimen. Unlike the previously studied response (increase in UTS) in the current response we see a overall positive correlation of average increase in toughness with plate thickness. The non-zero slopes of the lines indicate the presence of main effects due to plate thickness.
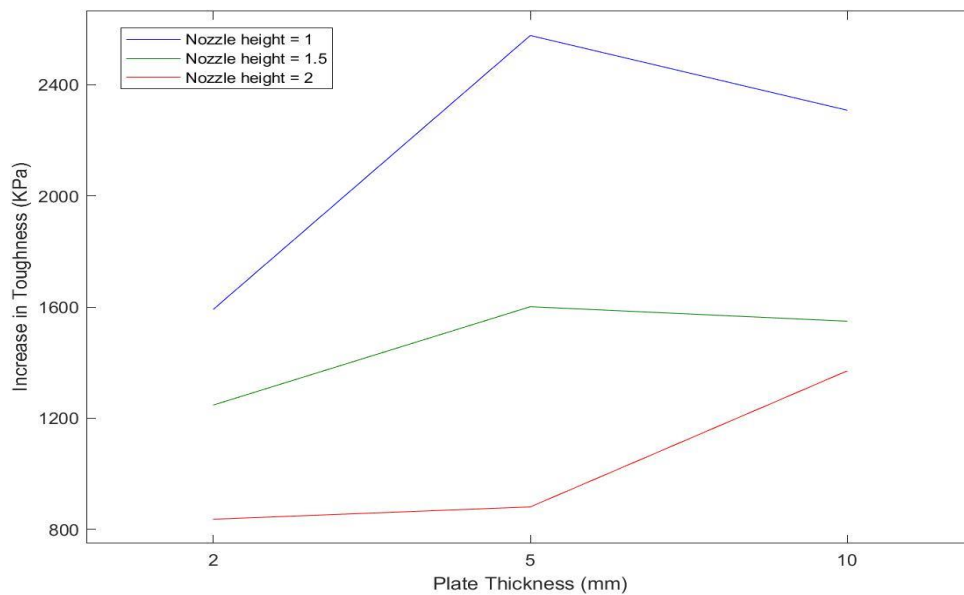

Figure 30. Interaction plot for increase in Toughness

71

The lines show similar trends, indicating that the interaction effects between nozzle height and plate thickness are not important. The above inferences can be further verified from the ANOVA results obtained in Table 6.

Table 6. ANOVA for the Increase in Toughness

Source	Degrees of Freedom	Type III Sums of Squares	Mean Square	F value	Pr > F
Nozzle Height (h)	2	9736406.44	4868203.2	24.65	<.0001
Plate thickness (t)	2	2420682.15	1210341.073	6.13	0.0051
h × t	4	1421927.11	355481.78	1.80	0.1502
Error	36	7108455.87	197457.11		
Corrected Total	44	20687471.57			

The ANOVA results show us that the nozzle height has the maximum contribution to the sums of squares. We also see that for the interaction effects the p-value (0.1502) > 0.01 (confidence level of 99%) confirming our inference from the interaction plots that the interaction effects are not important. But on comparing the p-value for the main effects due to nozzle height and plate thickness we see that these main effects are present for a confidence level of 99 %. Due to the absence of interaction effects, for future work the appropriate model is an additive model,

$$Y_{ijt} = \mu_{..} + \alpha_i + \beta_j + \varepsilon_{ijt} \tag{6}$$

with the assumptions that $\sum_i (\alpha)_i = 0$ and $\sum_j (\beta)_j = 0$, where α_i = main effects due to nozzle height, β_j = main effects due to plate thickness, $\mu_{..}$ = overall mean for all treatments and ε_{ijt} = error variable. But for our present study we will continue with our fitted full interaction model as given in Equation (4).

c) Increase in Fracture Toughness

From the interaction plots shown in Figure 31, three distinct lines can be seen corresponding to the different nozzle heights indicating the presence of main effects due to nozzle height. It is noticed that for an increase in nozzle height there is a significant fall in the average increase in fracture toughness. Also similar to the increase in toughness we see that for increase in fracture toughness, with an increase in plate thickness the average increase in fracture toughness goes up slightly. But this trend is not consistent for the 2mm nozzle height where the average increase in fracture toughness goes up from the 2mm plate thickness to the 10 mm plate thickness, but further falls from the 5mm plate to the 10 mm plate thickness.

Similar to the previous two response variables, from the ANOVA table it is seen that the nozzle height has the maximum contribution to the sums of squares. Also, for the interaction effects the p- value 0.6997>0.01 (99% confidence level) indicating the absence of interaction effects which was also observed from the interaction plots. On comparing the p-value for main effects due to plate thickness it is seen that even though the main effects are not seen for a 0.01 significance level, but the main effects are present at a 0.05 significance level and thus cannot be ignored. Thus, as only interaction effects are absent, the model for future work would be an additive model as given in Equation 6 with similar assumptions.
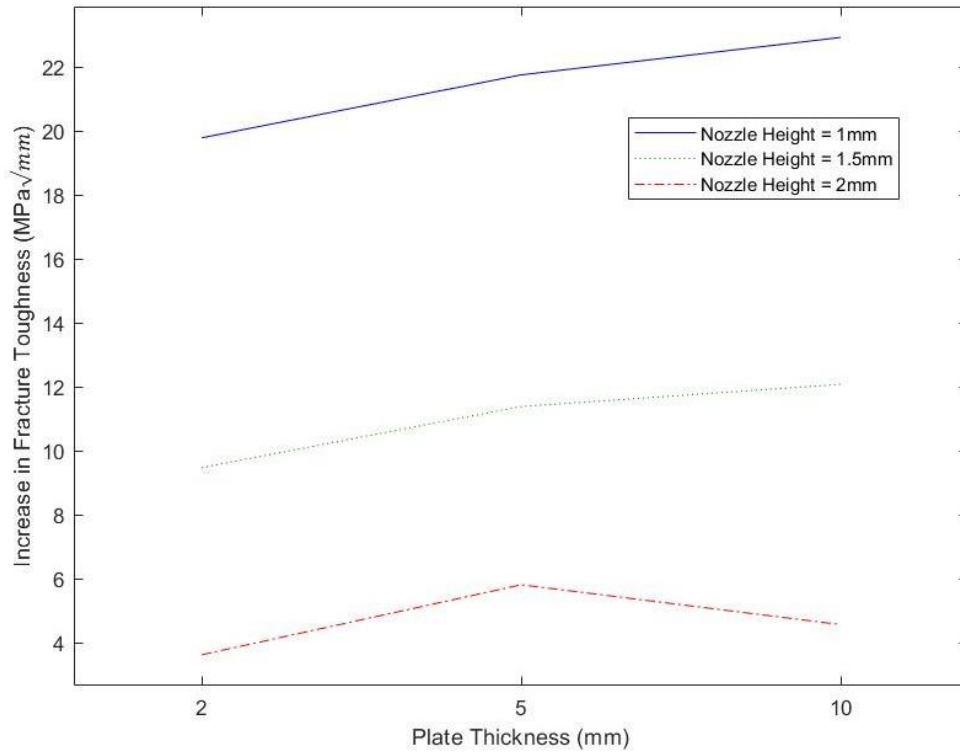
Figure 31. Interaction plot for increase in Fracture Toughness

Table 7. ANOVA for the Increase in Fracture Toughness

Source	Degrees of Freedom	Type III Sums of Squares	Mean Square	F value	Pr > F
Nozzle Height (h)	2	1298.94	649.46	241.8	<.0001
Plate thickness (t)	2	27.29	13.64	5.08	0.0178
h × t	4	5.94	1.484	0.55	0.6997
Error	18	48.35	2.686		
Corrected Total	26	1380.51			

Pairwise Comparisons.

A Tukey's pairwise comparison is done for both the response variables to obtain the significant factor levels at a 95% confidence level. This analysis of factor effects recognizes how the factor levels are statistically different from one another. For increase in UTS as main effects due to nozzle height and plate thickness are present for a 95% confidence level, thus a Tukey's pairwise comparison is done for different levels of nozzle height and plate thickness as shown in Figure 32. The vertical lines are used to connect two factor levels are not statistically different. We see from Figure 32 that all three nozzle heights have mean differences in the increase in UTS that are statistically different from each other. This suggests that as nozzle height is reduced from 2mm to 1.5mm to 1mm progressively higher increases in UTS can be achieved. But for the plate thickness it is seen that for a plate thickness of 2mm and 5mm the mean differences are not statistically distinguishable, also the plate thickness of 5mm and 10 mm have mean differences which are not statistically distinguishable. Thus, best results for increase in UTS can be achieved for a nozzle height of 1mm and plate thickness of 5mm.

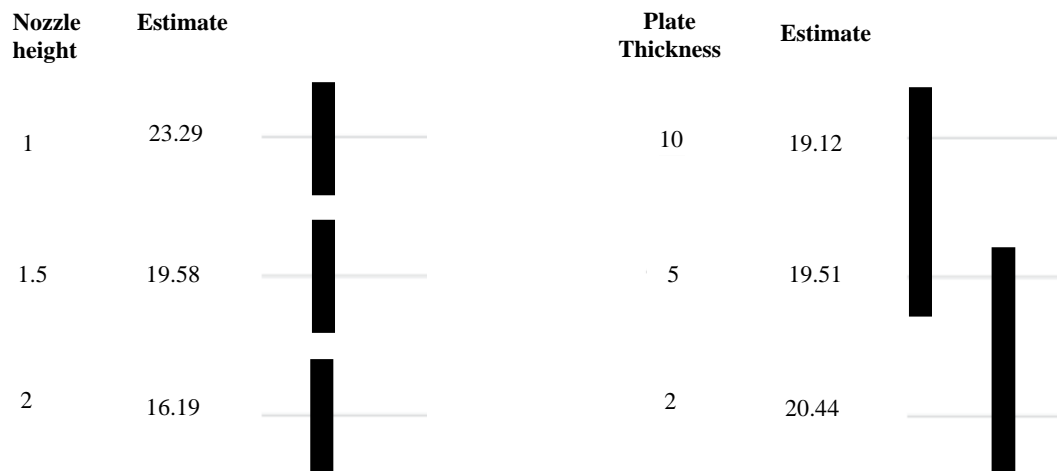| Nozzle height	Estimate		Plate Thickness	Estimate
1	23.29		10	19.12
1.5	19.58		5	19.51
2	16.19		2	20.44

Figure 32. Line plot for Tukey's Pairwise comparison: Increase in UTS

For the increase in toughness, we have 2 main effects namely, main effects due to nozzle height and main effects due to plate thickness. Figure 33 shows the line plots using Tukey's pairwise comparisons for the both the main effects. From the line plot for nozzle heights, we see that the three levels have mean differences in increase in toughness that are statistically different from each other. This implies that as nozzle height is reduced from 2mm to 1.5mm to 1mm we get progressively higher increase in toughness. From the line plot for plate thickness, we see that the mean differences in increase in toughness for the 5mm and 10mm plate are not statistically different. But we see that the 2mm plate has mean differences which are statistically different from the 5mm plate. This indicates that as the plate thickness is increased from 2mm to 5mm we see a higher increase in toughness. But between the 5mm plate and 10 mm plate the increase in toughness is not significant. Thus, maximum increase in toughness can be achieved for a 5mm plate or 10mm plate with 1mm nozzle height.

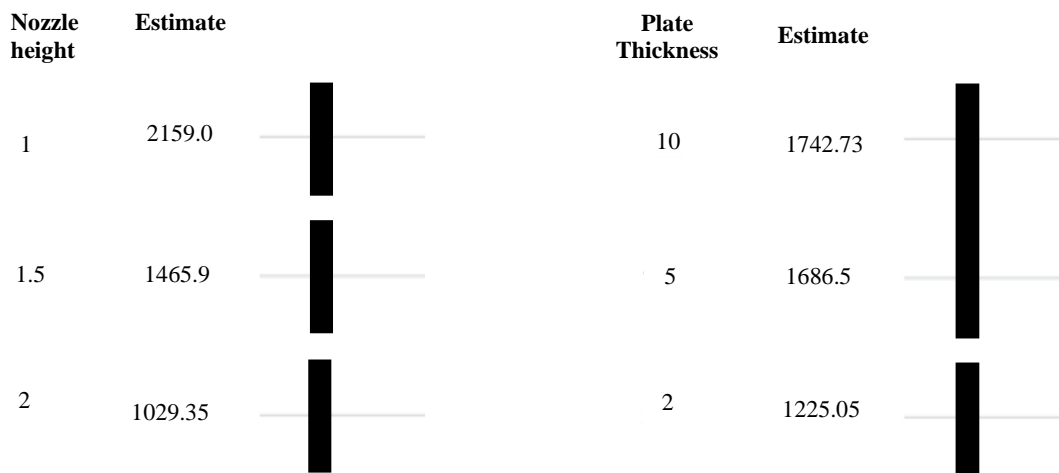| Nozzle height	Estimate		Plate Thickness	Estimate	
1	2159.0		10	1742.73	
1.5	1465.9		5	1686.5	
2	1029.35		2	1225.05	

Figure 33. Line plots for Tukey's Pairwise comparison: Increase in Toughness

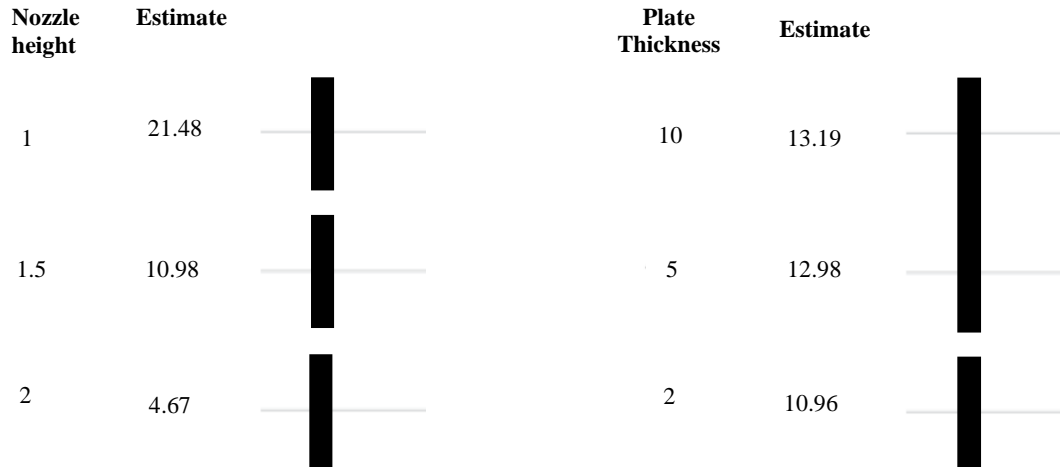| Nozzle height	Estimate		Plate Thickness	Estimate	
1	21.48		10	13.19	
1.5	10.98		5	12.98	
2	4.67		2	10.96	

Figure 34. Line plots for Tukey's Pairwise comparison: Increase in Fracture Toughness

Figure 34 shows Tukey's line plots for increase in fracture toughness. From the line plots for nozzle height, we see that all three nozzle heights have statistically distinguishable mean differences. It is seen that with an increase in nozzle height from 1mm to 1.5 mm to 2mm there is a fall in the increase in fracture toughness of the parts. From the line plots for plate thickness, the mean differences for the 5mm and 10mm plate thickness are not statistically distinguishable, but the mean differences for the 5mm plate and 2 mm plate are statistically distinguishable. Thus, it is seen that from a plate thickness of 2mm to 5mm we see a significant increase in increase in fracture toughness but as the plate thickness increases from 5mm to 10mm the increase is not statistically significant.

Optimized Design of Heater block assembly

Based on the Tukey's pairwise comparison it is seen that the optimized parameters for maximum UTS, toughness and fracture toughness were 1mm nozzle height and 5mm plate thickness. Based on these parameters the nozzle with a plate thickness of 5mm and nozzle height of 1mm would give the best results. The 5 mm plate thickness was chosen instead of the 10 mm plate because Tukey's pairwise comparison shows that the two are not statistically different (in terms of increase in average UTS, toughness and fracture toughness), also the 5 mm plate is lighter in weight, reducing the inertia during rapid movements due to lower mass, and it reaches the desired temperature in a shorter duration of time.

Chapter 5 Discussion

From the ANOVA results it is seen that for the response variable, increase in UTS, only main effects due to nozzle height and plate thickness are present. The maximum value for increase in UTS is achieved for the 1mm nozzle height, this means that as we reduce the nozzle height from 2mm to 1mm the increase in average UTS keeps going up. We see that for a nozzle height of 2mm there is an increase in average UTS from the reference specimen, but this increase is maximized for the 1mm nozzle height. For the plate thickness the Tukey's pairwise comparison shows that the 5mm and 10 mm plate thickness and the 2mm and 5mm plate thickness do not have statistically distinguishable mean differences, but the 2mm and 10mm plate thickness are statistically distinguishable. It is seen that the increase in UTS falls as the plate thickness increases from 2mm to 10mm, this can be explained since the 10m mm keeps the part at an elevated temperature for a longer duration of time as compared to the 2mm plate. Previous studies by Hart et al have shown that annealing for a longer duration of time leads to randomized coalescence and migration of voids, which sometimes leads to reduced values of increase in UTS. Thus, the best increase in UTS can be achieved for the 5mm plate thickness with the minimum weight for the plate.

On studying the ANOVA results for the second response variable (increase in Toughness) we see that the main effects due to both the nozzle height and plate thickness are present. There is a negative correlation of the average increase in toughness with the nozzle height, which is similar to the previous results. A decrease in nozzle height shows higher values of increase in average toughness, which signifies that for the 2mm nozzle height there is an increase in toughness, but this average increase is maximized for the 1mm nozzle height. With a change in the plate thickness, we see that the increase in average toughness goes up as the plate becomes thicker from 2mm to

5mm to 10mm. But the Tukey's line plots suggest that the mean differences between the 5mm plate and 10mm plate are not statistically significant thus one could choose a 5mm plate to achieve highest average increase in toughness.

ANOVA results for increase in fracture toughness show that the main effects due to nozzle heights and plate thickness are present. A significant fall in the average increase in fracture toughness is seen when the nozzle height increases from 1mm to 2mm. The fracture toughness of the parts is dependent on the layer where the Kapton tape is applied, thus when this layer is exposed to a higher temperature it leads to a higher increase in fracture toughness. Thus, it can be seen that the 1 mm nozzle height gives the best results for the increase in fracture toughness as compared to other factor levels. For the plate thickness, the increase in fracture toughness shows a slight positive trend as the plate thickness increases from 2mm to 10mm due to better reptation between the layers. But its has also been seen that for larger values of plate thickness the voids coalesce and migrate randomly due to longer durations of annealing, this may lead to a fall in the fracture toughness of the specimen if larger voids are present in the layer adjacent to the pre-crack in the specimen. Thus, a 5mm plate should be chosen as it leads to best results and void migration is not visible.

Apart from this a 5mm plate would be a better choice as it heats up much faster than the 10mm plate and reduces the inertia effects due to mass which lead to decreased geometric accuracy while fabricating the specimen. Thus, a nozzle height of 1mm and plate thickness of 5 mm gives us the best results for increased in UTS (118.6 %), increase in average toughness (558.6 %) and increase in average fracture toughness (106.9 %). The increase in average UTS and average toughness have been summarized in Table 8 for all factor level combinations.

Table 8. Percentage increase in average UTS and Toughness for different factor level combinations

Levels	Plate thickness (mm)	Nozzle height (mm)	Percentage increase in the average ultimate tensile strength (%)	Percentage increase in the average toughness (%)	Percentage increase in the average fracture toughness (%)
1	2	1	120.0	344.9	90.7
2	2	1.5	104.6	270.3	41.7
3	2	2	91.2	181.3	17.8
4	5	1	118.6	558.6	106.9
5	5	1.5	102.9	347.1	56
6	5	2	79.8	190.9	28.6
7	10	1	121.2	500.3	112.7
8	10	1.5	94.9	335.7	62.7
9	10	2	79.2	297.1	22.4

The increase in UTS and fracture toughness can also be characterized by looking at the cross-sectional images as seen in figure 35 and figure 36. Figure 35 shows the cross-sectional images of the failed surface for the reference and the different treatment combinations. It is seen that for the reference surface elongated voids are present between adjacent rasters. These elongated voids reduce the bond area and act as failure initiation zones leading to low values of UTS and fracture toughness in the reference specimen [134]. As we move from a nozzle height of 2mm to 1mm the voids coalesce together as shown in the Figure 35. This leads to an increased bond area between layers and reduces the failure initiation zones thus increasing the UTS and fracture toughness as we reduce nozzle height to 1mm. Also, during testing of the parts crazing is noticed on the parts that are printed using the modified heater block assembly which indicates a shift from laminar behavior towards homogeneity.

Figure 36 shows the changes in the void shapes and bond length for the different treatment combinations. It is seen that for the reference specimen we see equally spaced diamond shaped voids. But on studying the cross-sections of the specimen on which treatment combinations were applied we see that the void shape changes from diamond to a circular void. Similar changes in void shapes have been seen in previous studies with post process annealing thus indicating an analogous effect that takes place here. These diamond shaped voids have sharp edges which act as stress concentration points leading accentuating the premature failure of the reference specimen, but a shift towards circular voids reduces the stress intensity factor thus leading to a further increase in the strength of the parts when in-situ annealing is applied. We also see that for the 1mm nozzle height void migration takes places indicating that it is exposed to a higher temperature field as explained by the simulation results. Also, as the plate thickness increases to 10 mm not only is a shift in the regular pattern of the voids seen, but also the void coalescence leads to larger voids which are less in number.
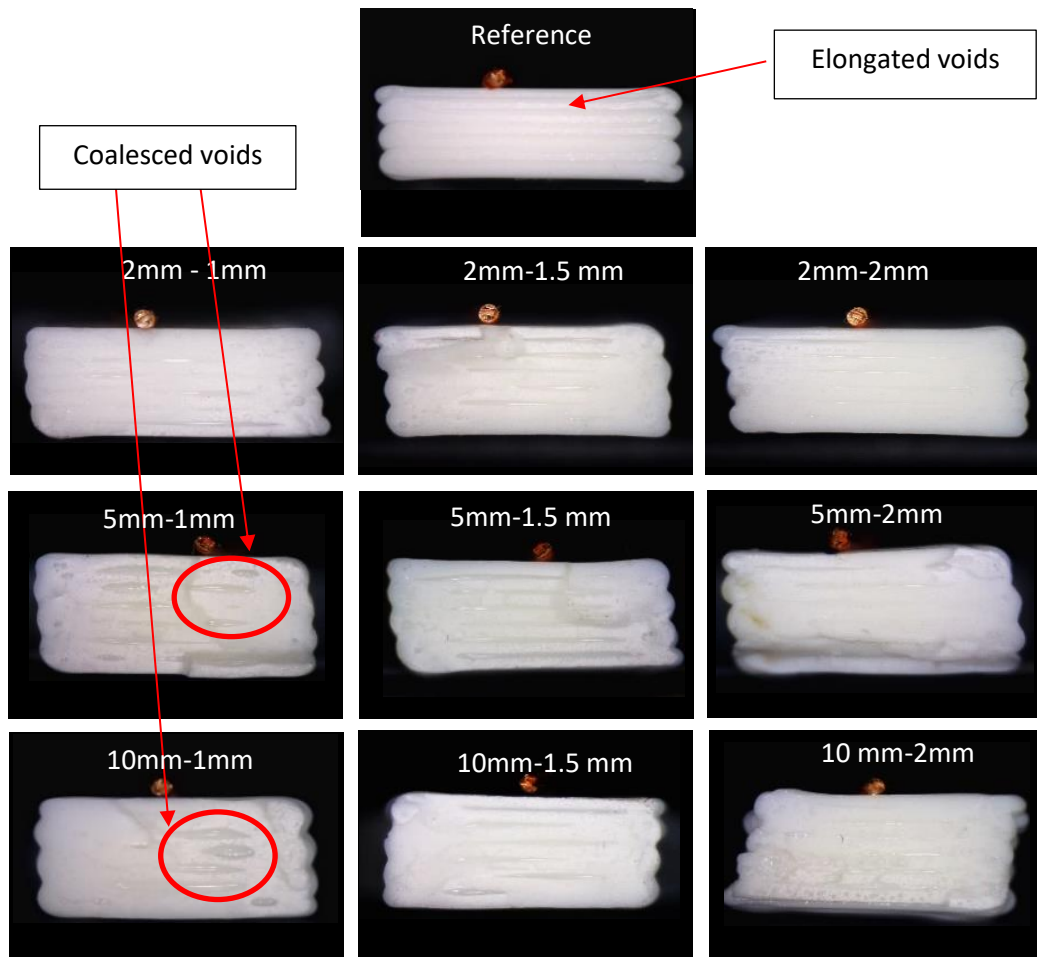
Figure 35. Failed surfaces for different treatment combinations

Figure 37 shows the stress-strain plots for different factor level combinations. The parts printed with the modified heater block assembly show enhanced stiffness (increased Young's Modulus) as compared to the reference values. Also, the failure mode of the specimen shifts from a brittle (reference specimen) to a more elastic-brittle failure when fabricated using the modified heater block assembly. In the study ductility and toughness show positive correlation with each other. An increase in ductility is seen with a decrease in nozzle height and an increase in the plate thickness.

The stress strain plots for the 5mm plate and 10mm plate show similar behavior with a noticeable brittle elastic failure at the 1 mm and 1.5mm nozzle height. For the 2mm plate we see enhanced stiffness and UTS, but the failure is more brittle as compared to the other two plates.
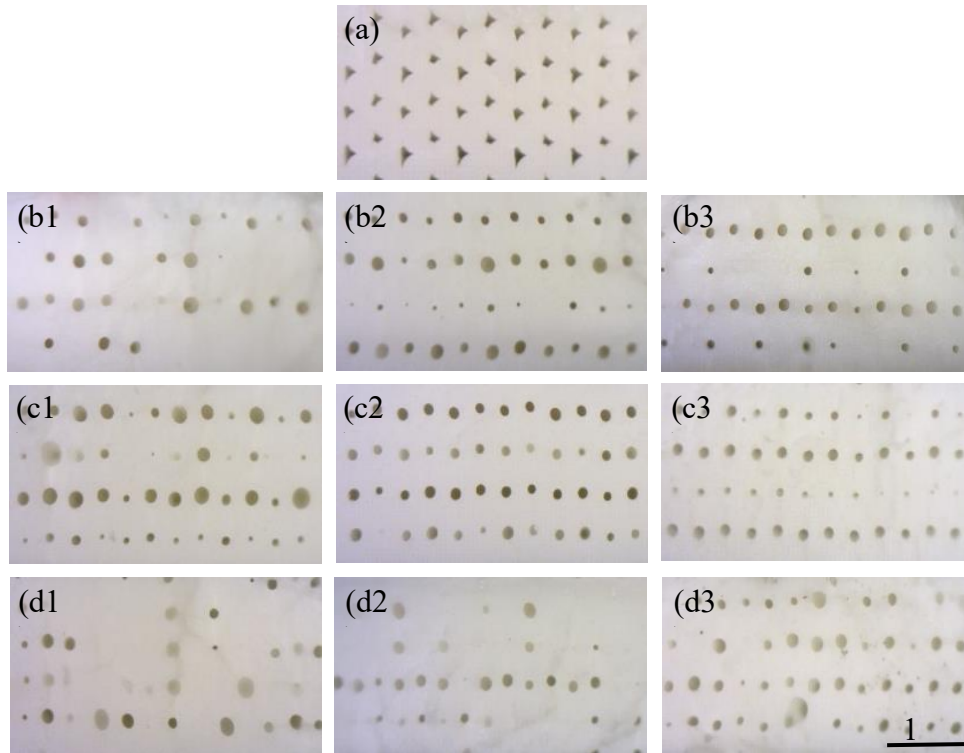

Figure 36. (a) Cross-section of a reference coupon. (b1) -(b3) Cross-section of a coupons printed with 2mm block with nozzle height of 1mm, 1.5mm and 2mm, respectively. Similarly, (c1) -(c3) and (d1)-(f4) are representative cross-sections of specimens printed with 5mm and 10 mm block with nozzle height of 1mm, 1.5mm and 2mm. All cross-sections are normal to build direction.

Another important inference that can be concluded from the stress-strain plots is that there is a change in the elastic modulus of the parts (considering only the Hookean region). For different plate thicknesses and nozzle heights, it is seen that the increase change in Young's modulus remains fairly constant with an average of 2144.4 ± 135.2 MPa. The treated parts Table 9 shows the average Young's modulus for the reference and the average Young's modulus of the parts printed using the novel print head.

Table 9. Young's Modulus of reference and treated parts as compared with bulk material

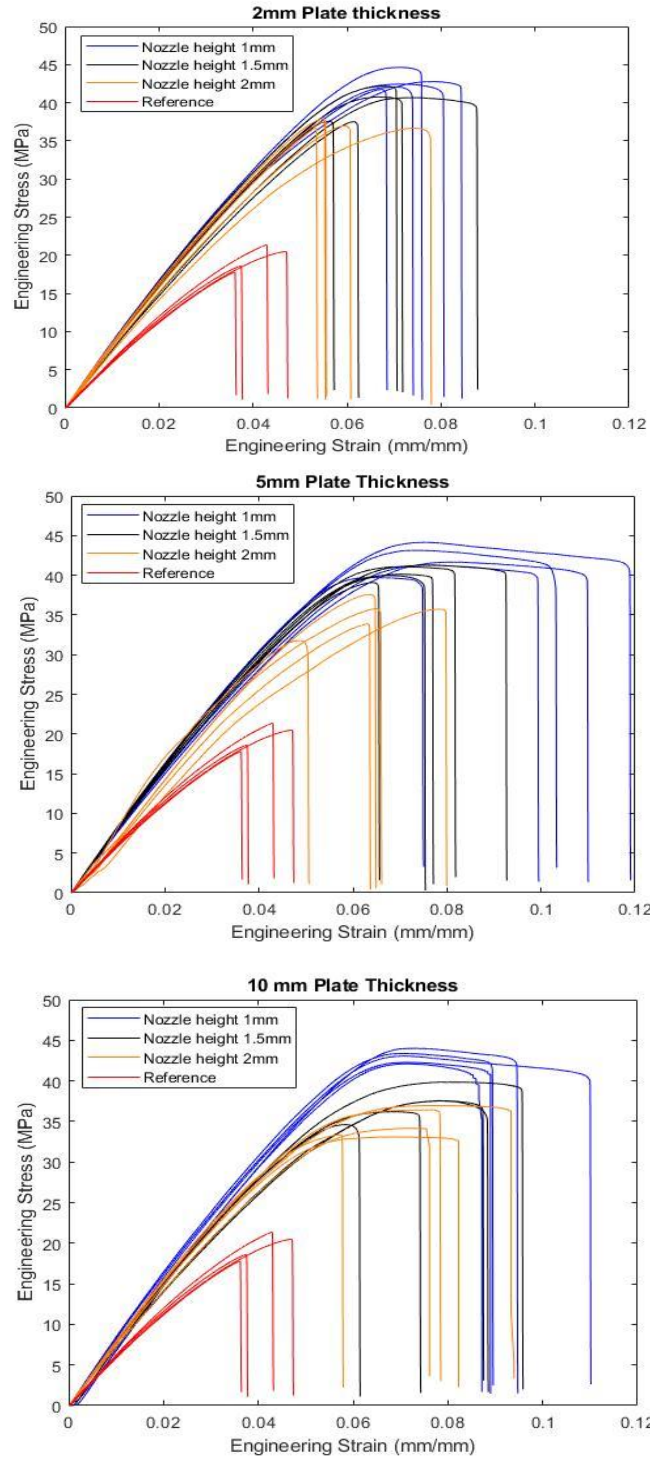|	Young's Modulus (MPa)	Compared to bulk material
Reference	1651.8 ± 48.72	45 %
Novel Print head	2144.4 ± 135.2 (77% increase)	60%

Figure 37. Stress-strain curves for specimen fabricated using different plate thicknesses and nozzle heights.

Chapter 6 Conclusion

In this study a novel modified heater block assembly was designed to increase the mechanical properties of FFF parts. A design of experiments approach was chosen to characterize the effect of the nozzle height and plate thickness on the two response variables (increase in average UTS, toughness and fracture toughness). In the 2-way full factorial design of experiments, 3 factor levels were chosen for each, the nozzle height and plate thickness. The specimens were tested under a tensile load to obtain the UTS and the area under the stress-strain curve was calculated to get the toughness, whereas ASTM 5045 was used to calculate the fracture toughness of CT specimen. The ANOVA results revealed the lack of interaction effects between nozzle height and plate thickness for both response variables. Only main effects due to nozzle height and plate thickness were seen to be present for all three response variables (99% confidence level). A finite volume simulations model was run to calculate the temperature field around the heater block assembly, this model helps to explain the effect of the nozzle height and plate thickness on the response variables. From Tukey's pairwise comparison it is seen that the optimized factor levels for maximum increase in UTS, toughness and fracture toughness are: 1mm nozzle height and 5mm plate thickness. For 1mm nozzle height and 5mm plate thickness, an increase in average UTS of 118.61 %, an increase in average toughness of 257.8% and an increase in fracture toughness of 106.9% was seen. Also, an average increase in Young's modulus by 77% of the specimens is seen as compared to the reference when the novel print head is used. Analysis of the cross-sectional images shows that the void shape changes from diamond to circular voids, thus indicating a reduction in stress concentrations. A study of failure surfaces shows that the failure mechanism moves from a interlaminar failure to a more homogeneous specimen behavior. The work done in this paper

provides the basis and understanding to the in-situ annealing process that occurs while using the novel modified heater block assembly. It provides a simple and elegant solution to print geometrically accurate parts with superior mechanical properties while solving the issues faced by previous studies. The modified heater block assembly provide a simple ready to use solution to improve mechanical strength at a fraction of the cost as that of other complicated heater block designs. From the current accomplished work, it is seen that on using the novel print head assembly the interlaminar bond quality improves drastically for FFF parts. Also, the advantage of FFF lies in fabricating larger complex geometries exposed to a combination of loading conditions (fatigue), thus it is essential to characterize the effect of the novel print head for similar conditions and also characterize their geometric accuracy.

References

1. O. Ivanova, C. Williams, T. Campbell, Additive manufacturing (AM) and nanotechnology promises and challenges, Rapid Prototyp. J. 19 (5) (2013) 353–364, https://doi.org/10.1108/RPJ-12-2011-0127.

2. D. Dimitrov, K. Schreve, N. de Beer, Advances in three dimensional printing – state of the art and future perspectives, Rapid Prototyping J. 12 (2006) 136–147.

3. I. Zein, D.W. Hutmacher, K.C. Tan, S.H. Teoh, Fused deposition modeling of novel scaffold architectures for tissue engineering applications, Biomaterials 4 (2000) 1169–1185

4. C.M. Gonz´alez-Henríquez, M.A. Sarabia-Vallejos, J. Rodriguez-Hernandez, Polymers for additive manufacturing and 4D-printing: materials, methodologies, and biomedical applications, Prog. Polym. Sci. 94 (2019) 57–116, https://doi. org/10.1016/j.progpolymsci.2019.03.001.

5. H. Wu, W.P. Fahy, S. Kim, H. Kim, N. Zhao, L. Pilato, A. Kafi, S. Bateman, J. H. Koo, Recent developments in polymers/polymer nanocomposites for additive manufacturing, Prog. Mater. Sci. 111 (2020), 100638, https://doi.org/10.1016/j.pmatsci.2020.100638.

6. N. Turner, R. Strong, and S. A. Gold, "A review of melt extrusion additive manufacturing processes: I. Process design and modeling," Rapid Prototyping Journal, vol. 20, pp. 192-204, 2014.

7. S.A.M. Tofail, E.P. Koumoulos, A. Bandyopadhyay, S. Bose, L. O'Donoghue, C. Charitidis, Additive manufacturing: scientific and technological challenges, market uptake and opportunities, Mater. Today 21 (1) (2018) 22–37, https://doi. org/10.1016/j.mattod.2017.07.001

8. Tanikella, N.G.; Wittbrodt, B.; Pearce, J.M. Tensile strength of commercial polymer materials for fused filament fabrication 3D printing. Addit. Manuf. 2017, 15, 40–47. [CrossRef]

9. Hill, N.; Haghi, M. Deposition direction-dependent failure criteria for fused deposition modeling polycarbonate. Rapid Prototyp. J. 2014, 20, 221–227. [CrossRef] Materials 2019, 12, 895 20 of 25

10. Chia, H.N.; Wu, B.M. Recent advances in 3D printing of biomaterials. J. Biol. Eng. 2015, 9, 1–14. [CrossRef][PubMed]

11. Arif, M.F.; Kumar, S.; Varadarajan, K.M.; Cantwell,W.J. Performance of biocompatible PEEK processed by fused deposition additive manufacturing. Mater. Des. 2018, 146, 249–259. [CrossRef]

12. Bagsik, A.; Schoppner, V. Mechanical properties of fused deposition modeling parts manufactured with ULTEM * 9085. ANTEC. 2011, 2, 1294–1298.

13. Mireles, J.; Espalin, D.; Roberson, D.; Zinniel, B.; Medina, F.;Wicker, R. Fused Deposition Modeling of Metals.In Proceedings of the Solid Freeform Fabrication Symposium, Austin, TX, USA, 6–8 August 2012; pp. 6–8.

14. D.T. Pham, R.S. Gault, A comparison of rapid prototyping technologies, Int. J. Mach. Tools Manuf. 38 (1998) 1257–1287.

15. J.-P. Kruth, M.C. Leu, T. Nakagawa, Progress in additive manufacturing and rapid prototyping, CIRP Ann. Manuf. Technol. 2 (1998) 525–540.

16. K.V. Wong, A. Hernandez, A review of additive manufacturing, ISRN Mech. Eng. (2012) pp. 208760:1-10.

17. B. Zhang, H. Liao, C. Coddet, Effects of processing parameters on properties of selective laser melting Mg–9% Al powder mixture, Mater. Des. 34 (2012) 753–758.

18. N.K. Tolochko, M.K. Arshinov, A.V. Gusarov, V.I. Titov, T. Laoui, L. Froyen, Mechanisms of selective laser sintering and heat transfer in Ti powder, Rapid Prototyp. J. 9 (2003) 314–326.

19. I. Gibson, D. Rosen, B. Stucker, Additive Manufacturing Technologies: 3D Printing, Rapid Prototyping, and Direct Digital Manufacturing, Springer, 2014.

20. Love, L.J.; Elliott, A.M.; Post, B.K.; Smith, R.J.; Blue, C.A. The importance of carbon fiber to polymer additive manufacturing. J. Mater. Res. 2014, 29, 1893–1898. [CrossRef]

21. Brischetto, S.; Ciano, A.; Ferro, C.G. A multipurpose modular drone with adjustable arms produced via the FDM additive manufacturing process. Curved Layer. Struct. 2016, 3. [CrossRef]

22. Chen, H.; Yang, X.; Chen, L.; Wang, Y.; Sun, Y. Application of FDM three-dimensional printing technology in the digital manufacture of custom edentulous mandible trays. Sci. Rep. 2016, 6, 1–6.

23. Arenas, L.F.; Walsh, F.C.; de León, C.P. 3D-Printing of Redox Flow Batteries for Energy Storage: A Rapid Prototype Laboratory Cell. ECS J. Solid State Sci. Technol. 2015, 4, 3080–3085. [CrossRef]

24. Ravari, M.K.; Kadkhodaei, M.; Badrossamay, M.; Rezaei, R. Numerical investigation on mechanical properties of cellular lattice structures fabricated by fused deposition modeling. Int. J. Mech. Sci. 2014, 88, 154–161. [CrossRef]

25. Tabacu, S.; Ducu, C. Experimental testing and numerical analysis of FDM multi-cell inserts and hybrid structures. Thin-Walled Struct. 2018, 129, 197–212. [CrossRef]

26. Brischetto, S.; Ferro, C.G.; Torre, R.; Maggiore, P. 3D FDM production and mechanical behavior of polymeric sandwich specimens embedding classical and honeycomb cores. Curved Layer. Struct. 2018, 5, 80–94. [CrossRef]

27. Hutmacher, D.W.; Schantz, T.; Zein, I.; Ng, K.W.; Teoh, S.H.; Tan, K.C. Mechanical properties and cell cultural response of polycaprolactone scaffolds designed and fabricated via fused deposition modeling. J. Biomed. Mater. Res. 2001, 55, 203–216. [CrossRef]

28. Chin Ang, K.; Fai Leong, K.; Kai Chua, C.; Chandrasekaran, M. Investigation of the mechanical properties and porosity relationships in fused deposition modelling-fabricated porous structures. Rapid Prototyp. J. 2006, 12, 100–105. [CrossRef]

29. Jones, R.; Haufe, P.; Sells, E.; Iravani, P.; Olliver, V.; Palmer, C.; Bowyer, A. Reprap—The replicating rapid prototype. Robotica 2011, 29, 177–191. [CrossRef]

30. Osborn, T.; Zhou, E.; Gerzeski, R.; Mollenhauer, D.; Tandon, G.P.; Whitney, T.J.; Iarve, E.V. Experimental and theoretical evaluation of stiffness properties of fused deposition modeling parts. In Proceedings of the American Society of Composites—30th Technical Conference, East Lansing, MI, USA, 28–30 September 2015.

31. Ahn, S.H.; Montero, M.; Odell, D.; Roundy, S.; Wright, P.K. Anisotropic material properties of fused deposition modeling ABS. Rapid Prototyp. J. 2002, 8, 248–257. [CrossRef]

32. Bellini, A.; Güçeri, S. Mechanical characterization of parts fabricated using fused deposition modeling. Rapid Prototyp. J. 2003, 9, 252–264

33.   C. Butler, R. McCullough, R. Pitchumani, and J. John Gillespie, "An Analysis of Mechanisms Governing Fusion Bonding of Thermoplastic Composites," Journal of Thermoplastic Composite Materials, vol. 11, pp. 338-363, 1998.

34.   R. P. Wool and K. M. O'Connor, "A theory crack healing in polymers," Journal of Applied Physics, vol. 52, pp. 5953-5963, 1981.

35.   F. Yang and R. Pitchumani, "Interlaminar Contact Development During Thermoplastic Fusion Bonding," Polymer Engineering and Science, vol. 42, pp. 424-438, 2002.

36. Theory of Healing at a Polymer-Polymer Interface 1115 Young Hwa Kim' and Richard P. Wool*

37. Butt, J.; Bhaskar, R. Investigating the Effects of Annealing on the Mechanical Properties of FFF-Printed Thermoplastics. *J. Manuf. Mater. Process.* 2020, *4*, 38. https://doi.org/10.3390/jmmp4020038

38. Rodríguez, J.F.; Thomas, J.P.; Renaud, J.E. Mechanical behavior of acrylonitrile butadiene styrene (ABS) fused deposition materials. Experimental investigation. Rapid Prototyp. J. 2001, 7, 148–158. [CrossRef]

39. Cuan-Urquizo, E.; Bhaskar, A. Flexural elasticity of woodpile lattice beams. Eur. J. Mech. A Solids 2018, 67, 187–199.

40. Cuan-Urquizo, E.; Yang, S.; Bhaskar, A. Mechanical characterisation of additively manufactured material having lattice microstructure. IOP Conf. Ser. Mater. Sci. Eng. 2015, 74, 12004.

41. D. P. Cole, J. C. Riddick, H. M. Iftekhar Jaim, K. E. Strawhecker, and N. E. Zander, "Interfacial mechanical behavior of 3D printed ABS," Journal of Applied Polymer Science, vol. 133, 2016.

42. Kazem Fayazbakhsh, Mobina Movahedi, Jordan Kalman,

43. The impact of defects on tensile properties of 3D printed parts manufactured by fused filament fabrication, Materials Today Communications, Volume 18, 2019, Pages 140-148, ISSN 2352-4928, https://doi.org/10.1016/j.mtcomm.2018.12.003.

44. Rajpurohit, S.R., Dave, H.K. Analysis of tensile strength of a fused filament fabricated PLA part using an open-source 3D printer. Int J Adv Manuf Technol 101, 1525–1536 (2019). https://doi.org/10.1007/s00170-018-3047-x

45. Nagendra G. Tanikella, Ben Wittbrodt, Joshua M. Pearce, Tensile strength of commercial polymer materials for fused filament fabrication 3D printing, Additive Manufacturing, Volume 15, 2017, Pages 40-47, ISSN 2214-8604, https://doi.org/10.1016/j.addma.2017.03.005.

46. G. Percoco, F. Lavecchia, and L. M. Galantucci, "Compressive Properties of FDM Rapid Prototypes Treated with a Low Cost Chemical Finishing," Journal of Applied Sciences, Engineering and Technology, vol. 4, pp. 3838-3842, October 1, 2012.

47. A. K. Sood, R. K. Ohdar, and S. S. Mahapatra, "Experimental investigation and empirical modelling of FDM process for compressive strength improvement," Journal of Advanced Research, vol. 3, pp. 81-90, 2012

48. Panda, B.N., Bahubalendruni, M.V.A.R. & Biswal, B.B. A general regression neural network approach for the evaluation of compressive strength of FDM prototypes. Neural Comput & Applic 26, 1129–1136 (2015). https://doi.org/10.1007/s00521-014-1788-5

49. C.S. Lee, S.G. Kim, H.J. Kim, S.H. Ahn, Measurement of anisotropic compressive strength of rapid prototyping parts, Journal of Materials Processing Technology, Volumes 187–188, 2007, Pages 627-630, ISSN 0924-0136, https://doi.org/10.1016/j.jmatprotec.2006.11.095.

50. Saty Dev, Rajeev Srivastava, Experimental investigation and optimization of FDM process parameters for material and mechanical strength, Materials Today: Proceedings, Volume 26, Part 2, 2020, Pages 1995-1999, ISSN 2214-7853, https://doi.org/10.1016/j.matpr.2020.02.435.

51. J. Fonseca, I.A. Ferreira, M.F.S.F. de Moura, M. Machado, J.L. Alves, Study of the interlaminar fracture under mode I loading on FFF printed parts, Composite Structures, Volume 214, 2019, Pages 316-324, ISSN 0263-8223, https://doi.org/10.1016/j.compstruct.2019.02.005.

52. G.D. Goh, V. Dikshit, A.P. Nagalingam, G.L. Goh, S. Agarwala, S.L. Sing, J. Wei, W.Y. Yeong, Characterization of mechanical properties and fracture mode of additively manufactured carbon fiber and glass fiber reinforced thermoplastics, Materials & Design, Volume 137, 2018, Pages 79-89, ISSN 0264-1275, https://doi.org/10.1016/j.matdes.2017.10.021.

53. Li, Q.; Zhao, W.; Li, Y.; Yang, W.; Wang, G. Flexural Properties and Fracture Behavior of CF/PEEK in Orthogonal Building Orientation by FDM: Microstructure and Mechanism. Polymers 2019, 11, 656. https://doi.org/10.3390/polym11040656

54. Torrado Perez, A.R.; Roberson, D.A.; Wicker, R.B. Fracture surface analysis of 3D-printed tensile specimens of novel ABS-based materials. J. Fail. Anal. Prev. 2014, 14, 343–353.

55. Aliheidari, N.; Tripuraneni, R.; Ameli, A.; Nadimpalli, S. Fracture resistance measurement of fused deposition modeling 3D printed polymers. Polym. Test. 2017, 60, 94–101.

56. Balderrama-Armendariz, C.O.; MacDonald, E.; Espalin, D.; Cortes-Saenz, D.; Wicker, R.; Maldonado-Macias, A. Torsion analysis of the anisotropic behavior of FDM technology. Int. J. Adv. Manuf. Technol. 2018, 96, 307–317

57. Domingo-Espin, M.; Borros, S.; Agullo, N.; Garcia-Granada, A.A.; Reyes, G. Influence of building parameters on the dynamic mechanical properties of polycarbonate fused deposition modeling parts. 3D Print. Addit. Manuf. 2014, 1, 70–77

58. Mohamed, O.A.; Masood, S.H.; Bhowmik, J.L. Experimental investigation for dynamic stiffness and dimensional accuracy of FDM manufactured part using IV-Optimal response surface design. Rapid Prototyp. J. 2017, 23, 736–749.

59. Mohamed, O.A.; Masood, S.H.; Bhowmik, J.L. Experimental investigations of process parameters influence on rheological behavior and dynamic mechanical properties of FDM manufactured parts. Mater. Manuf. Process. 2016, 31, 1983–1994

60. Jami, H.; Masood, S.H.; Song, W.Q. Dynamic response of FDM made ABS parts in different part orientations. Adv. Mater. Res. 2013, 748, 291–294.

61. P.G. de Gennes, Reptation of a polymer chain in the presence of fixed obstacles, J. Chem. Phys. 55 (1971) 572–579, https://doi.org/10.1063/1.1675789

62. S. Prager, M. Tirrell, The healing process at polymer–polymer interfaces, J. Chem. Phys. 75 (1981) 5194–5198, https://doi.org/10.1063/1.441871.

63. F. Yang, R. Pitchumani, Healing of thermoplastic polymers at an interface under nonisothermal conditions, Macromolecules 35 (2002) 3213–3224, https://doi.org/ 10.1021/ma010858o

64. M. Tirrell, Polymer self-diffusion in entangled systems, Rubber Chem. Technol. 57 (1984) 523–556, https://doi.org/10.5254/1.3536019. [31]

65. A. Lee, R.P. Wool, FT-IR study of orientation relaxation in uniaxially oriented monodisperse atactic polystyrenes, Macromolecules 19 (1986) 1063–1068, https://doi.org/10.1021/ma00158a022.

66. H. Watanabe, Viscoelasticity and dynamics of entangled polymers, Prog. Polym. Sci. 24 (1999) 1253–1403, https://doi.org/10.1016/S0079-6700(99)00029-5.

67. S.F. Edwards, Dynamics of polymers in solution and melts, Polymer. 26 (1985) 163–168, https://doi.org/10.1016/0032-3861(85)90025-4.

68. D.S. Pearson, G. Ver Strate, E. von Meerwall, F.C. Schilling, Viscosity and self-diffusion coefficient of linear polyethylene, Macromolecules. 20 (1987) 1133–1141, https://doi.org/10.1021/ma00171a044.

69. Lee, W.C.; Wei, C.C.; Chung, S.C. Chung, Development of a hybrid rapid prototyping system using low-cost fused deposition modeling and five-axis machining. J. Mater. Process. Technol. 2014, 214, 2366–2374. [CrossRef]

70. Chakraborty, D.; Reddy, B.A.; Choudhury, A.R. Extruder path generation for Curved Layer Fused Deposition Modeling. CAD Comput. Aided Des. 2008, 40, 235–243. [CrossRef]

71. Jin, Y.; Du, J.; He, Y.; Fu, G. Modeling and process planning for curved layer fused deposition. Int. J. Adv. Manuf. Technol. 2017, 91, 273–285. [CrossRef]

72. Lim, S.; Buswell, R.A.; Valentine, P.J.; Piker, D.; Austin, S.A.; De Kestelier, X. Modelling curved-layered printing paths for fabricating large-scale construction components. Addit. Manuf. 2016, 12, 216–230. [CrossRef] 39.

73. M. Heidari-Rarani, M. Rafiee-Afarani, A.M. Zahedi, Mechanical characterization of FDM 3D printing of continuous carbon fiber reinforced PLA composites, Composites Part B: Engineering, Volume 175, 2019, 107147, ISSN 1359-8368, https://doi.org/10.1016/j.compositesb.2019.107147.

74. Nabipour M, Akhoundi B. An experimental study of FDM parameters effects on tensile strength, density, and production time of ABS/Cu composites. Journal of Elastomers & Plastics. 2021;53(2):146-164. doi:10.1177/0095244320916838

75. Zhaobing Liu, Qian Lei, Shuaiqi Xing, Mechanical characteristics of wood, ceramic, metal and carbon fiber-based PLA composites fabricated by FDM, Journal of Materials Research and Technology, Volume 8, Issue 5, 2019, Pages 3741-3751, ISSN 2238-7854, https://doi.org/10.1016/j.jmrt.2019.06.034.

76. Durgun, I.; Ertan, R. Experimental investigation of FDM process for improvement of mechanical properties and production cost. Rapid Prototyp. J. 2014, 20, 228–235.

77. Montero, M.; Roundy, S.; Odell, D.; Ahn, S.-H.; Wright, P.K. Material characterization of fused deposition modeling (FDM) ABS by designed experiments. Soc. Manuf. Eng. 2001, 10, 1–21. 26.

78. Es-Said, O.; Foyos, J.; Noorani, R.; Mendelson, M.; Marloth, R.; Pregger, B. Effect of layer orientation on mechanical properties of rapid prototyped samples. Mater. Manuf. Process. 2000, 15, 107–122

79. Zaldivar, R.J.; Witkin, D.B.; McLouth, T.; Patel, D.N.; Schmitt, K.; Nokes, J.P. Influence of processing and orientation print effects on the mechanical and thermal behavior of 3D-Printed ULTEM®9085 Material. Addit. Manuf. 2017, 13, 71–80.

80. Wang, C.C.; Lin, T.-W.; Hu, S.-S. Optimizing the rapid prototyping process by integrating the Taguchi method with the Gray relational analysis. Rapid Prototyp. J. 2007, 13, 304–315.

81. Panda, S.K.; Padhee, S.; Anoop Kumar, S.; Mahapatra, S.S. Optimization of fused deposition modelling (FDM) process parameters using bacterial foraging technique. Intell. Inf. Manag. 2009, 1, 89–97

82. Górski, F.; Wichniarek, R.; Kuczko, W.; Andrzejewski, J. Experimental determination of critical orientation of ABS parts manufactured using fused deposition modelling technology. J. Mach. Eng. 2015, 15, 121–132.

83. Wittbrodt, B.; Pearce, J.M. The effects of PLA color on material properties of 3-D printed components. Addit. Manuf. 2015, 8, 110–116.

84. Deng, X.; Zeng, Z.; Peng, B.; Yan, S.; Ke, W. Mechanical properties optimization of poly-ether-ether-ketone via fused deposition modeling. Materials 2018, 11, 216.

85. Uddin, M.S.; Sidek, M.F.R.; Faizal, M.A.; Ghomashchi, R.; Pramanik, A. Evaluating Mechanical Properties and Failure Mechanisms of Fused Deposition Modeling Acrylonitrile Butadiene Styrene Parts. J. Manuf. Sci. Eng. 2017, 139, 81018.

86. Sood, A.K.; Ohdar, R.K.; Mahapatra, S.S. Parametric appraisal of mechanical property of fused deposition modelling processed parts. Mater. Des. 2010, 31, 287–295

87. Hart, K.R.; Wetzel, E.D. Fracture behavior of additively manufactured acrylonitrile butadiene styrene (ABS) materials. Eng. Fract. Mech. 2017, 177, 1–13.

88. Yang, X. Tian, D. Li, Y. Cao, F. Zhao, C. Shi, Influence of thermal processing conditions in 3D printing on the crystallinity and mechanical properties of PEEK material, J. Mater. Process. Technol. 248 (2017) 1–7, https://doi.org/10.1016/j.jmatprotec.2017.04.027

89. Kuo, CC., Wu, YR., Li, MH. *et al.* Minimizing warpage of ABS prototypes built with low-cost fused deposition modeling machine using developed closed-chamber and optimal process parameters. *Int J Adv Manuf Technol* 101, 593–602 (2019). https://doi.org/10.1007/s00170-018-2969-7

90. Abinesh Kurapatti Ravi, Anagh Deshpande, Keng H. Hsu, An in-process laser localized pre-deposition heating approach to inter-layer bond strengthening in extrusion based polymer additive manufacturing, Journal of Manufacturing Processes, Volume 24, Part 1,2016,Pages 179-185,ISSN 1526-6125,https://doi.org/10.1016/j.jmapro.2016.08.007.

91. Vidya Kishore, Christine Ajinjeru, Andrzej Nycz, Brian Post, John Lindahl, Vlastimil Kunc, Chad Duty, Infrared preheating to improve interlayer strength of big area additive manufacturing (BAAM) components, Additive Manufacturing, Volume 14, 2017, Pages 7-12, ISSN 2214-8604, https://doi.org/10.1016/j.addma.2016.11.008.

92.C.B.Sweeney,B.A.Lackey,M.J.Pospisil,T.C.Achee,V.K.Hicks,A.G.Moran,B.R.Teipel,M.A.Saed,M.J.Green,Welding of 3D printed carbon nanotube polymer composites by locally induced microwave heating, Sci.Adv.3(6)(2017).

93.   Darshan Ravoori, Hardikkumar Prajapati, Viswajit Talluru, Ashfaq Adnan, Ankur Jain, Nozzle-integrated pre-deposition and post-deposition heating of previously deposited layers in polymer extrusion based additive manufacturing, Additive Manufacturing, Volume 28, 2019, Pages 719-726, ISSN 2214-8604, https://doi.org/10.1016/j.addma.2019.06.006.

94. Chin-Cheng Shih, Matthew Burnette, David Staack, Jyhwen Wang, Bruce L. Tai, Effects of cold plasma treatment on interlayer bonding strength in FFF process, Additive Manufacturing, Volume 25, 2019, Pages 104-111, ISSN 2214-8604, https://doi.org/10.1016/j.addma.2018.11.005.

95. Wu, W.; Geng, P.; Li, G.; Zhao, D.; Zhang, H.; Zhao, J. Influence of Layer Thickness and Raster Angle on the Mechanical Properties of 3D-Printed PEEK and a Comparative Mechanical Study between PEEK and ABS. Materials 2015, 8, 5834-5846. https://doi.org/10.3390/ma8095271

96. Boschetto, A.; Giordano, V.; Veniali, F. 3D roughness profile model in fused deposition modelling. Rapid Prototyp. J. 2013, 19, 240–252

97. Jason T Cantrell, Sean Rohde, David Damiani, Rishi Gurnani, Luke DiSandro, Josh Anton, Andie Young, Alex Jerez, Douglas Steinbach, Calvin Kroese, Peter G Ifju, (2017) "Experimental characterization of the mechanical properties of 3DPrinted ABS and polycarbonate parts", Rapid Prototyping Journal, Vol. 23 Issue: 4, doi: 10.1108/RPJ-03-2016-0042

98. Stratasys Inc., in Ultem 9085 (product information, 2016). http://www.stratasys.com/materials/fdm/ultem-9085. Accessed 31 March 2021.

99. Hao, W.; Liu, Y.; Zhou, H.; Chen, H.; Fang, D. Preparation and characterization of 3D printed continuous carbon fiber reinforced thermosetting composites. Polym. Test. 2018, 65, 29–34. [CrossRef]

100. Akhoundi, B.; Behravesh, A.H.; Bagheri Saed, A. Improving mechanical properties of continuous fiber-reinforced thermoplastic composites produced by FDM 3D printer.

101. Li, N.Y.; Li, Y.G.; Liu, S.T. Rapid prototyping of continuous carbon fiber reinforced polylactic acid composites by 3D printing. J. Mater. Process. Technol. 2016, 238, 218–225. (In English)

102. Oztan, C.; Karkkainen, R.; Fittipaldi, M.; Nygren, G.; Roberson, L.; Lane, M.; Celik, E. Microstructure and mechanical properties of three dimensional-printed continuous fiber composites. J. Compos. Mater.

103. Matsuzaki, R.; Ueda, M.; Namiki, M.; Jeong, T.K.; Asahara, H.; Horiguchi, K.; Nakamura, T.; Todoroki, A.; Hirano, Y. Three-dimensional printing of continuous-fiber composites by in-nozzle impregnation. Sci. Rep. 2016, 6, 23058.

104. N. Li, Y. Li, S. Liu, Rapid prototyping of continuous carbonfiber reinforced poly-lactic acid composites by 3D printing, J. Mater. Process. Technol. 238 (2016)218–225,http://dx.doi.org/10.1016/j.jmatprotec.2016.07.025.

105. C. Yang, X. Tian, T. Liu, Y. Cao, D. Li, 3D printing for continuousfiber reinforcedthermoplastic composites: mechanism and performance, Rapid Prototyp. J. 23(2017) 209–215,http://dx.doi.org/10.1108/RPJ-08-2015-0098

106. J.M. Gardner, G. Sauti, J.-W. Kim, R.J. Cano, R.A. Wincheski, E.V. Barrera, Additivemanufacturing of multifunctional components using high density carbon nanotubeyarnfilaments, SAMPE Conf. Proc. Long Beach, CA, 2016.

107. Bastian Brenken, Eduardo Barocio, Anthony Favaloro, Vlastimil Kunc, R. Byron Pipes, Fused filament fabrication of fiber-reinforced polymers: A review, Additive Manufacturing, Volume 21, 2018, Pages 1-16, ISSN 2214-8604, https://doi.org/10.1016/j.addma.2018.01.002. (https://www.sciencedirect.com/science/article/pii/S2214860417304475)

108. Torrado, A.R.; Shemelya, C.M.; English, J.D.; Lin, Y.; Wicker, R.B.; Roberson, D.A. Characterizing the effect of additives to ABS on the mechanical property anisotropy of specimens fabricated by material extrusion 3D printing. Addit. Manuf. 2015, 6, 16–29.

109. Rasselet, D.; Caro-Bretelle, A.-S.; Taguet, A.; Lopez-Cuesta, J.-M. Reactive Compatibilization of PLA/PA11 Blends and Their Application in Additive Manufacturing. Materials 2019, 12, 485

110. Wu, J.; Chen, N.; Bai, F.; Wang, Q. Preparation of poly(vinyl alcohol)/poly(lactic acid)/hydroxyapatite bioactive nanocomposites for fused deposition modeling.

111. Haryńska, A.; Kucinska-Lipka, J.; Sulowska, A.; Gubanska, I.; Kostrzewa, M.; Janik, H. Medical-Grade PCL Based Polyurethane System for FDM 3D Printing—Characterization and Fabrication

112. Levenhagen, N.P.; Dadmun, M.D. Interlayer diffusion of surface segregating additives to improve the isotropy of fused deposition modeling products. Polymer 2018, 152, 35–41. [CrossRef]Materials 2019, 12, 1664 35 of 35 212.

113. Levenhagen, N.P.; Dadmun, M.D. Bimodal molecular weight samples improve the isotropy of 3D printed polymeric samples. Polymer 2017, 122, 232–241. [CrossRef] 213.

114. Levenhagen, N.P.; Dadmun, M.D. Improving Interlayer Adhesion in 3D Printing with Surface Segregating Additives: Improving the Isotropy of Acrylonitrile-Butadiene-Styrene Parts. ACS Appl. Polym. Mater

115. Galantucci, L.M., Lavecchia, F., and Percoco, G., 2009. Experimental study aiming to enhance the surface finish of fused deposition modelled parts. CIRP Annals – Manufacturing Technology, 58, 189–192. doi:10.1016/j.cirp. 2009.03.071

116. Li, J. Interfacial studies on the O3 modified carbon fiber-reinforced polyamide 6 composites. *Appl. Surf. Sci.* 2008, *255*, 2822–2824

117. Galantucci, L. M., Lavecchia, F., and Percoco, G., 2010. Quantitative analysis of a chemical treatment to reduce roughness of parts fabricated using fused deposition modeling. CIRP Annals – Manufacturing Technology, 59, 247–250. doi:10.1016/j.cirp.2010.03.074

118. N. Jayanth, P. Senthil & C. Prakash (2018) Effect of chemical treatment on tensile strength and surface roughness of 3D-printed ABS using the FDM process, Virtual and Physical Prototyping, 13:3, 155-163, DOI: 10.1080/17452759.2018.1449565

119. Lederle, F.; Meyer, F.; Brunotte, G.P.; Kaldun, C.; Hübner, E.G. Improved mechanical properties of 3D-printed parts by fused deposition modeling processed under the exclusion of oxygen. *Prog. Addit. Manuf.* 2016, *2*, 3–7

120. Chen, L.; Zhang, X.; Wang, Y.; Osswald, T.A. Laser polishing of Cu/PLA composite parts fabricated by fused deposition modeling: Analysis of surface finish and mechanical properties.

121. Rane, R. Enhancing Tensile Strength of FDM parts using Thermal Annealing and Uniaxial Pressure. University of Texas at Arlington

122. Rane, Rhugdhrivya; Kulkarni, Akhilesh; Prajapati, Hardikkumar; Taylor, Robert; Jain, Ankur; Chen, Victoria. 2020. "Post-Process Effects of Isothermal Annealing and Initially Applied Static Uniaxial Loading on the Ultimate Tensile Strength of Fused Filament Fabrication Parts" Materials 13, no. 2: 352. https://doi.org/10.3390/ma13020352

123. Singh, S.; Singh, M.; Prakash, C.; Gupta, M.K.; Mia, M.; Singh, R. Optimization and reliability analysis to improve surface quality and mechanical characteristics of heat-treated fused filament fabricated parts. *Int. J. Adv. Manuf. Technol.* 2019, *102*, 1521–1536

124. Hong, J.H.; Yu, T.; Chen, Z.; Park, S.J.; Kim, Y.H. Improvement of flexural strength and compressive strength by heat treatment of PLA filament for 3D-printing. *Mod. Phys. Lett. B* 2019, *33*, 1940025.

125. Kevin R. Hart, Ryan M. Dunn, Jennifer M. Sietins, Clara M. Hofmeister Mock, Michael E. Mackay, Eric D. Wetzel, Increased fracture toughness of additively manufactured amorphous thermoplastics via thermal annealing, Polymer,Volume 144,2018,Pages 192-204,ISSN 0032-3861,https://doi.org/10.1016/j.polymer.2018.04.024.

126. Kevin R. Hart, Ryan M. Dunn, Eric D. Wetzel, Increased fracture toughness of additively manufactured semi-crystalline thermoplastics via thermal annealing, Polymer, Volume 211, 2020, 123091, ISSN 0032-3861, https://doi.org/10.1016/j.polymer.2020.123091.

127. Hart, K.R., Dunn, R.M. and Wetzel, E.D. (2020), Tough, Additively Manufactured Structures Fabricated with Dual-Thermoplastic Filaments. Adv. Eng. Mater., 22: 1901184. https://doi.org/10.1002/adem.201901184

128. Maidin, S.; Muhamad, M.K.; Pei, E. Feasibility study of ultrasonic frequency application on fdm to improve parts surface finish. J. Teknol. 2015, 77, 27–35.

129. Tofangchi, A.; Han, P.; Izquierdo, J.; Iyengar, A.; Hsu, K. Effect of Ultrasonic Vibration on Interlayer Adhesion in Fused Filament Fabrication 3D Printed ABS. Polymers 2019, 11, 315.

130. Wu, W.; Jiang, J.; Jiang, H.; Liu, W.; Li, G.; Wang, B.; Tang, M.; Zhao, J. Improving bending and dynamic mechanics performance of 3D printing through ultrasonic strengthening. Mater. Lett.

131. https://www.astm.org/Standards/D638.htm, last accessed August 2020

132. Stafford, Jason & Walsh, Ed & Egan, Vanessa. (2009). Characterizing convective heat transfer using infrared thermography and the heated-thin-foil technique. Measurement Science and Technology. 20. 105401. 10.1088/0957-0233/20/10/105401.

133. Dean, A. M., and Voss, D., 2000, Design and Analysis of Experiments (Springer Texts in Statistics), Springer-Verlag, New York

134. Robert M. Taylor, Edgar Mares, Rhugdhrivya Rane and Mike Love. "Process Calibration for Elastically Scaled 3D Printed Models Using Fused Deposition Modeling," AIAA 2019-1768. AIAA Scitech 2019 Forum. January 2019.